Liquid and Ice Cloud Microphysics in the CSU General Circulation Model. Part II: Impact on Cloudiness, the Earth's Radiation Budget, and the General Circulation of the Atmosphere

LAURA D. FOWLER AND DAVID A. RANDALL

Department of Atmospheric Science, Colorado State University, Fort Collins, Colorado

(Manuscript received 30 March 1994, in final form 21 July 1995)

ABSTRACT

A prognostic equation for the mass of condensate associated with large-scale cloudiness introduces a direct coupling between the atmospheric moisture budget and the radiation budget through interactive cloud amounts and cloud optical properties. We have compared the cloudiness, the top-of-the-atmosphere and surface radiation budgets, the radiative forcing of clouds, and the atmospheric general circulation simulated with the Colorado State University general circulation model with and without such a prognostic cloud parameterization. In the EAULIQ run, the radiative effects of cloud water, cloud ice, and snow are considered; those of rain are omitted. The cloud optical depth and cloud infrared emissivity depend on the cloud water, cloud ice, and snow paths predicted by a bulk cloud microphysics parameterization. In the CONTROL run, a conventional large-scale condensation scheme is used. Cloud optical properties depend on the mean cloud temperatures. Results are presented in terms of January and July means.

Comparisons with data from the International Satellite Cloud Climatology Project and the Earth Radiation Budget Experiment show that EAULIQ yields improved simulations of the geographical distributions of the simulated cloudiness, the top-of-the-atmosphere radiation budget, and the longwave and shortwave cloud radiative forcings. Differences between EAULIQ and CONTROL are largest in the Tropics and are mostly due to a decrease, in the EAULIQ run, in the amount and optical thickness of upper-tropospheric clouds. In particular, the cold bias in the outgoing longwave radiation and the overestimation of the planetary albedo obtained in the CONTROL run over the tropical convective regions are substantially reduced. Differences in the radiative and latent heating rates between EAULIQ and CONTROL lead to some improvements in the atmospheric general circulation simulated by EAULIQ when compared against statistics on the observed circulation assembled by the European Centre for Medium-Range Weather Forecasts. When compared to CONTROL, EAULIQ yields a warmer troposphere except below 8 km between 30°N and 30°S. The mean meridional circulation is significantly weakened in the EAULIQ run.

1. Introduction

Parameterization of cloudiness and its interactions with dynamical, thermodynamic, and radiative processes has been an ongoing challenge since the very first atmospheric general circulation models (GCMs), as reviewed by Fowler et al. (1996, hereafter Part I). Difficulties in appropriately describing the temporal and spatial variability of cloudiness and its optical properties are gradually being resolved. More realistic simulations of the coupling between clouds and the atmospheric hydrologic cycle are being obtained (Le Treut and Li 1988; Del Genio and Yao 1988; Roeckner et al. 1990; Smith 1990; Ose 1993; Tiedtke 1993; Part I). The studies mentioned above employ a prognostic equation for the mass of water condensate. Condensed water may remain stored in the atmosphere for a finite time instead of being removed immediately in the form of rain or snow, hence allowing clouds to have finite lifetimes. Efforts are being made to develop parameterizations of the cloud optical properties of water, ice, and mixed-phase clouds as functions of the cloud water path, providing the basic coupling between the simulated hydrologic cycle and radiation (Slingo 1989; Ebert and Curry 1992; Hu and Stamnes 1993; Sun and Shine 1994).

The impact of prescribed versus interactive cloud optical depths and infrared emissivities has been the object of numerous studies aimed at improving the simulation of climate using GCMs. Interactive cloud optical properties introduce important feedbacks between latent and radiative heating, thus altering both the climate and its sensitivity due to external forcings. For example, Ramanathan et al. (1983) demonstrated that parameterizing the emissivities of cirrus clouds as functions of the water path, instead of prescribing cirrus as black, produced major improve-

Corresponding author address: Dr. Laura D. Fowler, Department of Atmospheric Science, Colorado State University, Fort Collins, CO 80523.

ments in the zonal winds, temperatures, and radiation budget of the NCAR Community Climate Model. Liquid water dependent versus fixed cloud optics have been shown to produce significantly different albedo distributions, especially in the Tropics (Charlock and Ramanathan 1985). Senior and Mitchell (1993) concluded that the warming of the surface–troposphere system due to a doubling of CO_2 is reduced when prescribed cloud optical properties are replaced by cloud optical properties that depend on liquid and ice water paths.

In this paper, we analyze the impact of liquid and ice cloud microphysics and interactive cloud optical properties on the cloudiness, the earth radiation budget (ERB), the longwave and shortwave cloud radiative forcings, and the atmospheric general circulation simulated with the Colorado State University General Circulation Model (CSU GCM). Two numerical simulations are discussed. EAULIQ refers to the climate simulation obtained with the CSU GCM including a bulk cloud microphysics parameterization, as described in Part I. When cloud formation is predicted, the cloud optical depth and infrared emissivity depend on the predicted cloud water, cloud ice, and snow paths. The climate simulation obtained with the standard version of the CSU GCM is hereafter referred to as CONTROL. In CONTROL, large-scale condensation is instantaneously removed from the atmosphere in the form of rain, which can evaporate as it falls. Ice effects in stratiform clouds are not included. The cloud optical depth and infrared emissivity depend on the mean cloud temperature (Harshvardhan et al. 1989).

In section 2, we briefly outline the major differences in the parameterization of the prediction of cloud formation and cloud optical properties between EAULIQ and CONTROL. Section 3 describes the design of the numerical simulations. Section 4 presents differences in the global distribution of cloudiness and the effects of prognostic cloud water and cloud ice on the simulated cloud optical properties. Cloud amounts obtained with EAULIQ and CONTROL are compared with data from the International Satellite Cloud Climatology Project (ISCCP; Rossow and Schiffer 1983). The effects of interactive cloud optical properties on the simulated top-of-the-atmosphere longwave and shortwave cloud radiative forcings and simulated outgoing longwave radiation and planetary albedo are described in section 5. We also compare the simulated top-of-the-atmosphere radiation budget components with those derived from the ERB Experiment (ERBE; Barkstrom and Smith 1986). Differences in the atmospheric general circulation between EAULIQ and CONTROL are discussed in section 6. Section 7 summarizes our results and highlights improvements that prognostic equations for the condensed species have made in the simulation of the top-of-the-atmosphere radiation budget and cloudiness.

2. Cloud–radiation interactions

The cloud microphysics parameterization is discussed in detail in Part I. Briefly, the scheme is based on bulk cloud microphysics equations developed for mesoscale models, as described by Lin et al. (1983) and Rutledge and Hobbs (1983, 1984). It encompasses five prognostic variables for the masses of water vapor, cloud water, cloud ice, rain, and snow. The tendencies due to microphysical interactions among the five water species (condensation/evaporation, deposition/sublimation, autoconversion and collection processes, Bergeron–Findeisen process) are computed using an implicit time-differencing scheme. The precipitation rates for rain and snow are computed using an explicit scheme with a small time step (two minutes). Water clouds are assumed to form in the temperature range $T \geqslant T_0$, while ice clouds are predicted to form if $T < T_{00}$. Here T_0 and T_{00} are set equal to 0°C and −20°C, respectively. Mixed-phase clouds occur in the temperature window ($T_{00} < T \leqslant T_0$) over which supercooled cloud water and cloud ice coexist and the Bergeron–Findeisen process is active.

The parameterization of radiative transfer at infrared and solar wavelengths follows Harshvardhan et al. (1987). The upward and downward clear-sky longwave fluxes are computed using the concept of broadband absorptivity. The radiative transfer scheme takes into account the molecular absorption and emission by H_2O following the transmission approach of Chou (1984), and also the effects of the water vapor continuum (Roberts et al. 1976). The CO_2 absorptance model is based on the work of Chou and Peng (1983). Absorption by O_3 follows the model of Rodgers (1968). Cloudy fluxes are obtained by computing the probability of a clear line of sight between each model layer and all other layers, the ground, and the top of the atmosphere. This probability varies depending on the choice of cloud overlap, that is, maximum or random.

At solar wavelengths, the computation of the clear-sky fluxes follows the formulation of Lacis and Hansen (1974) for the molecular absorption by H_2O, CO_2, O_3, and Rayleigh scattering. The major difference with Lacis and Hansen (1974) is in the treatment of scattering by clouds, which is dependent upon the solar zenith angle. Assuming that the cloud optical depth, single scattering albedo, and asymmetry factor of a cloudy layer are known, cloudy fluxes are computed using the Delta–Eddington approximation (Joseph et al. 1976).

In both climate simulations discussed here, no clouds are allowed to exist in the two highest model layers, which are located between 100 mb and the model's top located at 51.3 mb.

The EAULIQ simulation does not include fractional cloudiness at this time. Radiatively active clouds are assumed to form above the planetary boundary layer (PBL) when and where the total amount of condensate exceeds 10^{-5} kg kg^{-1}. Their cloud fraction is set equal

to 1. This finite threshold is necessary to hinder the formation of optically very thin upper-tropospheric clouds. This assumption will not be necessary when fractional cloudiness will become part of our cloud microphysics parameterization. Then the cloud fraction will become a function of the cloud water and cloud ice mixing ratios, and small amounts of condensate will lead to fractional cloud amounts much less than unity (Xu and Randall 1994).

In CONTROL, stratiform clouds are predicted to form above the PBL if the relative humidity reaches or exceeds 100% or if convective clouds penetrate atmospheric layers above 500 mb to simulate the formation of stratiform anvils at the tops of cumulus towers. The fraction of large-scale condensation clouds is set equal to 1, whereas that of "convective anvils" is scaled by the convective mass flux, following the relation:

$$C = 75 \times M_c, \tag{1}$$

where C is the fractional cloudiness and M_c is the convective mass flux at the top of the PBL expressed in kilograms per square meter per second. Historically, the anvil fraction was set equal to 1, as for large-scale stratiform clouds (Harshvardhan et al. 1989; Randall et al. 1989, 1991). Modifications made to the cumulus parameterization to include a prognostic equation for the turbulent kinetic energy (Randall and Pan 1993) led to more frequent cumulus activity and the too frequent formation of thick tropical convective anvils. In Eq. (1), the constant 75 was chosen so that the globally averaged outgoing infrared radiation is in reasonable agreement with satellite observations.

In both EAULIQ and CONTROL, the parameterization of PBL clouds follows the formulation of Harshvardhan et al. (1989); their cloud fraction is assumed to be one when they are more than 12.5 mb deep, and decreases linearly to zero as their pressure thickness decreases from 12.5 mb to zero.

In EAULIQ, the optical effects of cloud water, cloud ice, and snow are considered; those of rain are omitted. As explained in Part I, the optical effects of rain are neglected because rain falls more rapidly through the atmosphere than snow, and "rain" clouds would then have much shorter lifetimes. The computation of the cloud optical depth τ_x, where x refers to the subscript c for cloud water, i for cloud ice, and s for snow, and cloud infrared emissivity (ϵ_x) as functions of cloud water, cloud ice, and snow path (W_x, with dimensions of mass per unit area) follows the formulation of Stephens (1978) and Harshvardhan et al. (1989), respectively; that is,

$$\tau_x = \frac{3}{2}\frac{W_x}{r_e} \tag{2}$$

and

$$\epsilon_x = 1 - \exp(-\kappa\tau_x). \tag{3}$$

The effective radius r_e is set equal to 10 μm for cloud water, 30 μm for cloud ice, and 1000 μm for snow. The infrared absorption coefficient κ is set to 0.75 $m^2\ g^{-1}$. The single scattering albedo for cloud water (ω_{0c}) is set equal to 0.99, while those for both cloud ice (ω_{0i}) and snow (ω_{0s}) are set to 0.98. The asymmetry factors for cloud water (g_c), cloud ice (g_i), and snow (g_s) are assumed to be 0.85, 0.75, and 0.75.

Following Rockel et al. (1991), we assume that the total optical depth of mixed-phase clouds (τ_m) is the sum of the optical depths of cloud water, cloud ice, and snow:

$$\tau_m = \tau_c + \tau_i + \tau_s. \tag{4}$$

The infrared emissivity of mixed-phase clouds (ϵ_m) is computed using (3), but with $\tau_x = \tau_m$. The single scattering albedo (ω_{0m}) and asymmetry factor (g_m) of mixed-phase clouds are computed using weighted averages; that is,

$$\omega_{0m} = \frac{\omega_{0c}g_c\tau_c + \omega_{0i}g_i\tau_i + \omega_{0s}g_s\tau_s}{g_c\tau_c + g_i\tau_i + g_s\tau_s} \tag{5}$$

and

$$g_m = \frac{g_c\tau_c + g_i\tau_i + g_s\tau_s}{\tau_m}. \tag{6}$$

In CONTROL, the cloud optical depth (τ) and infrared emissivity (ϵ) are computed as functions of the cloud mean temperature, following the formulation proposed by Harshvardhan et al. (1989); that is,

$$\tau = \begin{cases} a(T_c - T_0)^2\Delta p_c, & T_0 \leq T_c \leq -10°\text{C} \\ b\Delta p_c, & 0°\text{C} \leq T_c \end{cases} \tag{7}$$

with a linear interpolation of τ between $-10°$ and 0°C. The emissivity ϵ is obtained using (3), but with $\tau_x = \tau$, as given by (7). In (7), T_c is the mean cloud temperature, T_0 is set to -82.5°C following the observational study by Platt and Harshvardhan (1988), and Δp_c is the pressure thickness of the cloud. The constants a and b are set to 2.0×10^{-6} and 0.08, respectively, and were obtained by trial and error using satellite data (Harshvardhan et al. 1989). For optically thick anvil clouds associated with convection, (7) does not apply. Instead, we use the temperature independent coefficient $b = 0.16$ in the equation $\tau = b\Delta p_c$.

3. Computational design

The CSU GCM is described in Part I. Briefly, the CSU GCM is a 17-level gridpoint model with a horizontal resolution of 4° in latitude by 5° longitude. The vertical discretization is based on a modified σ coordinate in which the planetary boundary layer (PBL) is the bottom layer of the model (Suarez et al. 1983). The cumulus parameterization is a modified version of the original Arakawa–Schubert cumulus parameterization

(Arakawa and Schubert 1974; Randall and Pan 1993). Large-scale condensation processes are treated using the bulk cloud microphysics parameterization described in Part I. Coupling between convection and large-scale condensation is made through detrainment at the tops of cumulus towers.

EAULIQ and CONTROL are the same climate simulations as those used in Part I to describe the impact of liquid and ice cloud microphysics on the global distributions of the various components of the atmospheric moisture budget. As a reminder, the CSU GCM was run through an annual cycle preceded by a three-month spinup. The starting date corresponds to 1 October of a previous long-term climate simulation performed without cloud microphysics. CONTROL was run through a full annual cycle starting with the same initial conditions as EAULIQ, but with the cloud microphysics parameterization and interactive cloud optical properties turned off. Results are presented in terms of January and July monthly averages.

To evaluate our results, we used monthly averaged total cloud amounts and monthly averaged high-, middle-, and low-level cloud amount estimates from the ISCCP level C2 cloud data products (Rossow and Schiffer 1991), and also monthly averaged radiation budget data obtained from the ERBE scanner instruments (Barkstrom and Smith 1986). Both datasets were obtained on a 2.5° by 2.5° grid and were interpolated to match the GCM's coarser grid. We computed January and July ensemble averages for 1985–1988. This is the time period during which both ISCCP and ERBE observations were available simultaneously. Also, we use ECMWF analyses (Hollingsworth et al. 1986; Trenberth and Olson 1988) obtained from the National Center for Atmospheric Research to quantitatively compare selected fields of the atmospheric general circulation against observed circulation statistics. The ECMWF data were collected four times daily by the global radiosonde network and satellite remote sensing and analyzed on a global grid using a "first guess" field generated from a six-hour forecast by the ECMWF model. We computed January and July ensemble averages of the ECMWF data by combining the 0000 and 1200 UTC data and interpolated the 2.5° by 2.5° data onto the coarser grid of the CSU GCM. Finally, we used surface shortwave radiation budget estimates derived by Li and Leighton (1993) and surface longwave radiation budget estimates derived by Gupta et al. (1993) to evaluate the surface radiation budget simulated with EAULIQ and CONTROL.

4. Cloudiness

ISCCP-C2 cloud products are most reliable between 60°N and 60°S. At higher latitudes, the detection of cloudy pixels against the background scene is difficult because the difference between the cloud-top and surface temperatures and between the cloud and surface albedos is small. Hence, we focus our comparison between 60°N and 60°S.

In Fig. 1, we compare the July global distribution of the monthly averaged cloudiness (C) simulated with EAULIQ and CONTROL against ISCCP-C2 data between 60°N and 60°S. Figure 2 is as Fig. 1 but for the monthly averaged difference in C between January and July. Figure 3 shows the zonally averaged distribution of C, along with that of the cumulus incidence obtained with EAULIQ and CONTROL, also between 60°N and 60°S for January and July. The partitioning of C between high-, middle-, and low-level cloud amounts is shown in Fig. 4. Following the classification of Rossow and Schiffer (1991), high- and low-level clouds are defined as clouds with cloud-top pressures less than 440 mb and greater than 680 mb, respectively. Middle-level clouds are defined as clouds with cloud-top pressures between 680 and 440 mb. In comparing the amounts of simulated high-, middle-, and low-level clouds against satellite data, our goal is to show the change in the vertical distribution of the model cloudiness between EAULIQ and CONTROL relative to the satellite-derived cloud estimates. Global averages of the various cloud amounts are listed in Table 1 for January and July.

Satellite-derived cloud amounts indicate nearly overcast conditions above the major storm-track regions over the North Pacific and North Atlantic Oceans and the entire Southern Ocean in July. Cloud amounts in excess of 80% are also observed above the well-known convective activity centers in July, that is, Central America and Southeast Asia. Low-level stratiform clouds associated with subsidence over cold water along the western coasts of the continents, that is, California and Northern Africa, are also clearly evident. Mostly cloud-free regions are found over the subtropical oceans and the major desert regions. In many cases, there is a very sharp boundary between nearly overcast and cloud-free regions.

A comparison of EAULIQ and CONTROL shows that EAULIQ produces a significant improvement in the geographical distribution of C relative to the observations. In particular, and in contrast to CONTROL, EAULIQ produces sharper boundaries between cloudy and cloud-free areas, whereas CONTROL leads to cloud amounts in excess of 80% over most of the globe. Despite the significant improvement in the simulation of C with EAULIQ, there remain significant differences between the simulated and observed distributions of cloudiness. EAULIQ has a tendency to overestimate C over the tropical convective centers, the high pressure belts over eastern Europe and China, as well as over the Southern Ocean. In contrast, EAULIQ underestimates C over the middle-latitude storm track regions over the North Atlantic and North Pacific Oceans. Also the inability of the CSU GCM to simulate realistically high PBL cloud amounts along the western

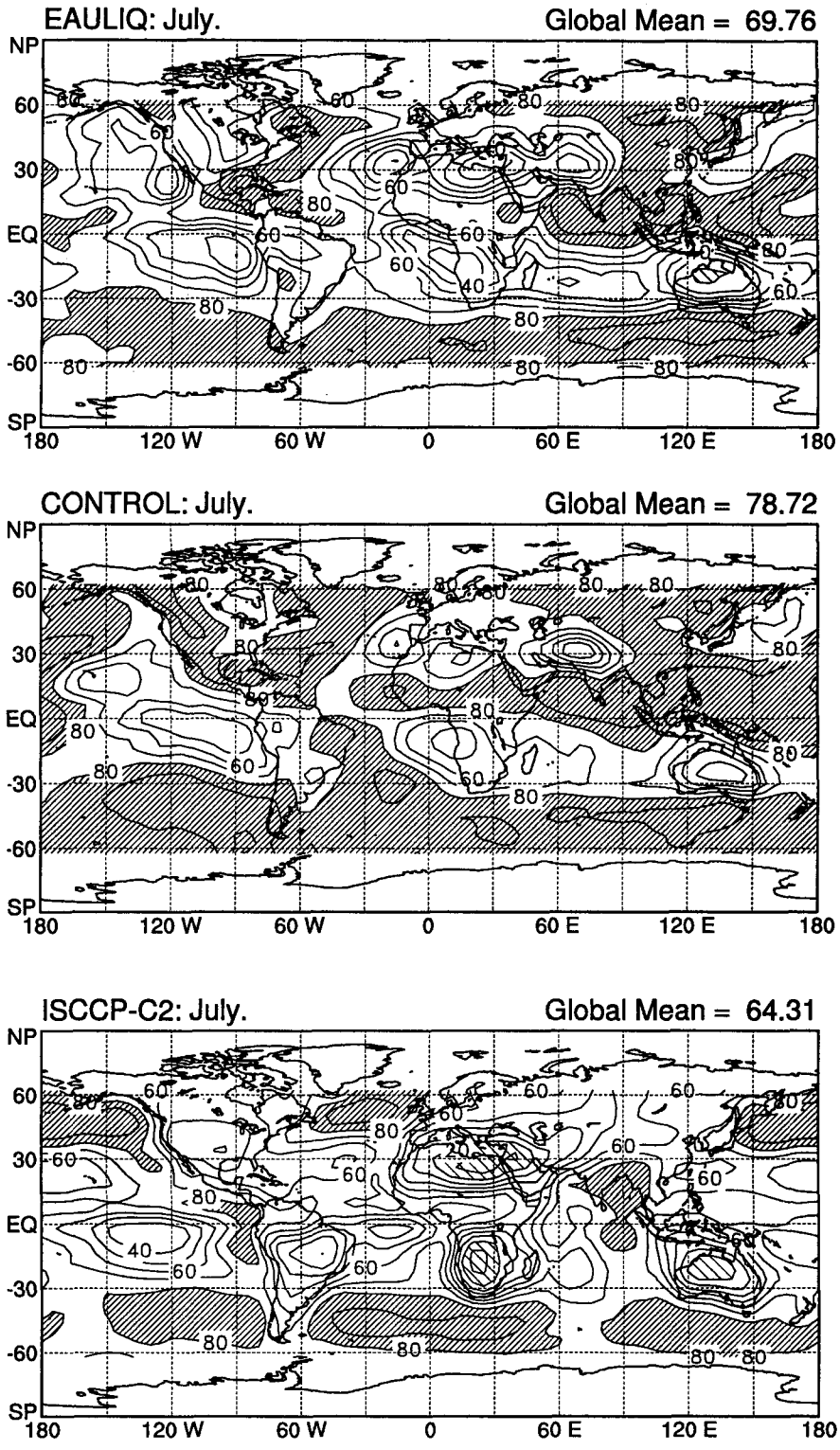

FIG. 1. Geographical distributions of the monthly averaged total cloud amount simulated with EAULIQ, CONTROL, and derived from the ISCCP-C2 dataset between 60°N and 60°S for July. Units are in percent and contour intervals are every 10%. Light shading corresponds to values less than 20%, and heavy shading corresponds to values greater than 80%.

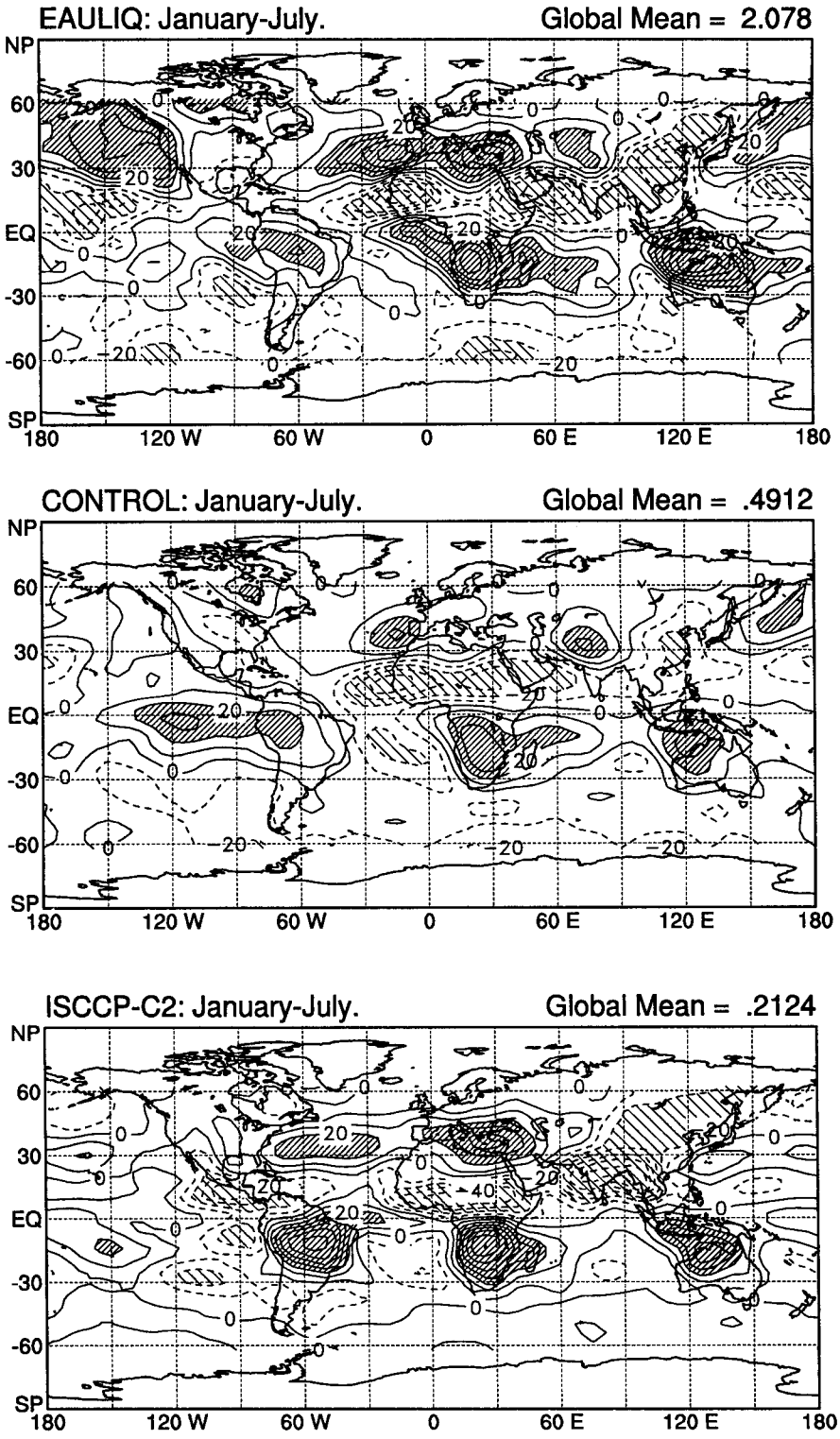

FIG. 2. Geographical distributions of the difference January minus July in the monthly averaged total cloud amount simulated with EAULIQ, CONTROL, and derived from the ISCCP-C2 dataset between 60°N and 60°S. Units are in percent and contour intervals are every 10%. Light shading corresponds to values less than −20%, and heavy shading corresponds to values greater than 20%.

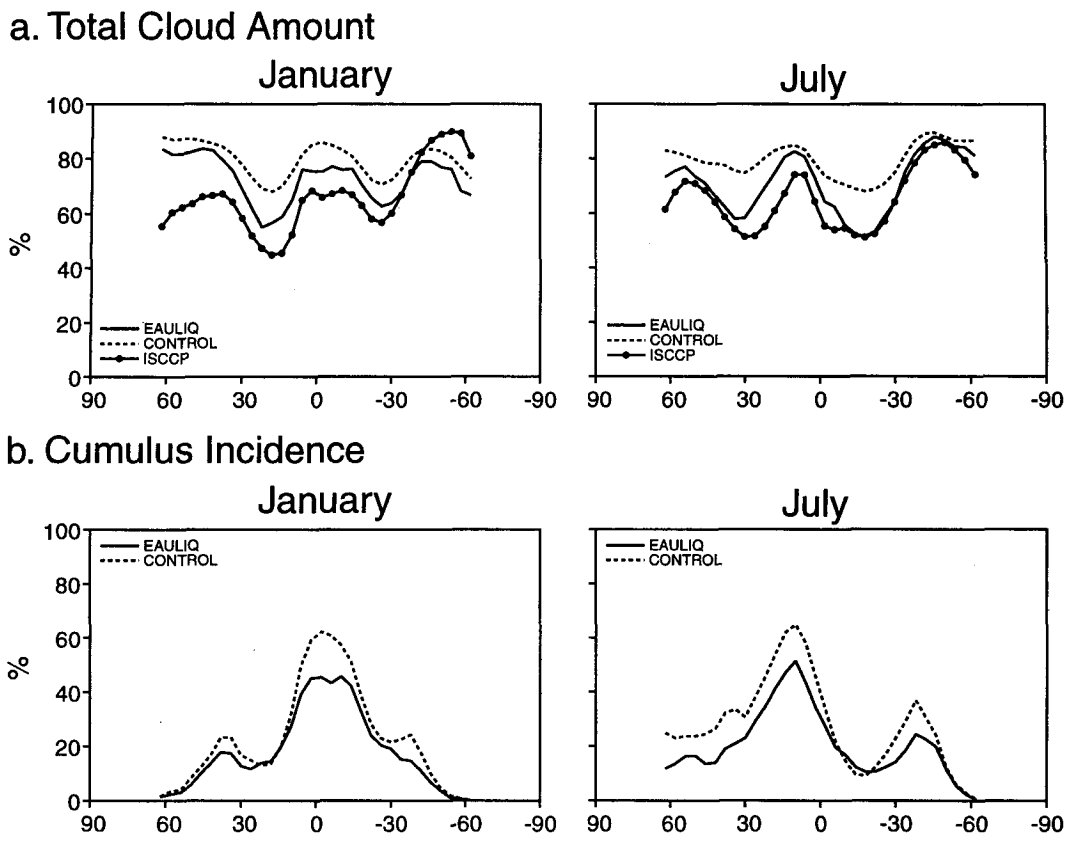

FIG. 3. Zonally averaged distributions of the monthly averaged (a) total cloud amount and (b) cumulus incidence simulated by EAULIQ and CONTROL and derived from the ISCCP-C2 dataset between 60°N and 60°S for January and July. Units are in percent.

coasts of the continents makes the subtropical cloud-free regions to extend too close to the shore.

In Fig. 2, ISCCP-C2 data clearly show the seasonal shift in the tropical convective activity centers between January and July, especially over land. The southern migration of the ITCZ between January and July leads to an increase in C over South America, southern Africa, Malaysia, and northern Australia, whereas C decreases over Central America, equatorial Africa, and Southeast Asia. The presence of a stable arctic air mass over eastern Europe and China also leads to a decrease in C between July and January, whereas the increased cyclonic activity over the oceans in January produces an increase in C in the Northern Hemisphere, especially over the Atlantic Ocean. We obtain much weaker seasonal variations of C in CONTROL because CONTROL yields fractional cloud amounts in excess of 80% over most of the globe in both January and July. In particular, the seasonal shift in C over the Tropics is poorly simulated. In contrast, the seasonal cycle of C is better simulated with EAULIQ, although its magnitude is strongly overestimated in the Northern Hemisphere over land and oceans and underestimated over the chief tropical convective activity regions.

Table 1 shows that the globally averaged total cloud amount drops from 79.3% in CONTROL to 71.5% in EAULIQ in January (and from 78.6% to 69.4% in July), which improves the agreement with the ISCCP-C2 estimated amounts of 62.7% in January and 62.9% in July, respectively. As seen in Fig. 3, the decrease in C between EAULIQ and CONTROL takes place everywhere except in middle and high latitudes in the winter hemisphere. Looking at Fig. 4, it is apparent that the decrease in high-level clouds (on a global average, −15.1% in January and −16.7% in July) strongly contributes to the decrease in C in EAULIQ. The reduction in high-level clouds is, in turn, due to the decreased cumulus incidence between EAULIQ and CONTROL, as seen in Fig. 3. The decrease in convective activity, and hence the decreased formation of tropical stratiform anvils, is discussed further in the next section. On a global average, the amounts of middle- and low-level clouds actually increase by 11.1% and 5.9% in January and 13% and 5.7% in July, indicating an increase of the relative humidity of the middle troposphere and PBL in EAULIQ. The small difference in the low-level cloud amount between EAULIQ and CONTROL results because the param-

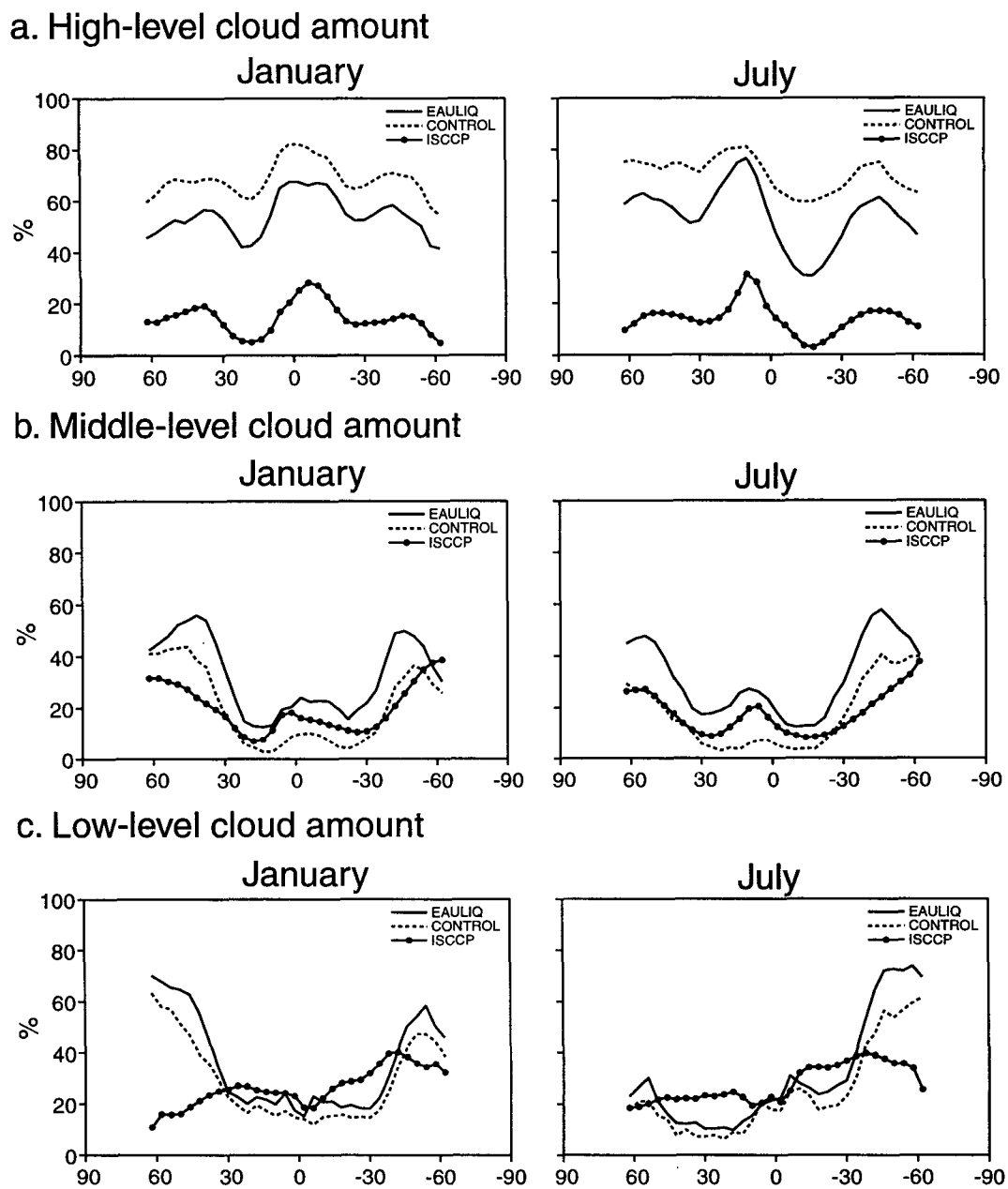

FIG. 4. Zonally averaged distributions of the monthly averaged (a) high-, (b) middle-, and (c) low-level cloud amounts simulated with EAULIQ and CONTROL, and derived from the ISCCP-C2 dataset between 60°N and 60°S, for January and July. Units are in percent.

eterization of PBL clouds is the same in both runs. Differences between simulated and satellite-derived middle-level clouds, and at some latitudes low-level clouds, may result because ISCCP underestimates the amount of middle- and low-level clouds when high-level clouds are present above them. We did not account for that "obscuring" effect in the computation of the simulated middle- and low-level cloud fractions.

The change in the vertical distribution of cloudiness is best seen in Fig. 5. In this figure, the latitude–height cross sections of C and its difference (EAULIQ minus CONTROL) are plotted for July. Two main differences between EAULIQ and CONTROL stand out. EAULIQ yields a decrease in C in the upper troposphere and an increase in C in the middle and low troposphere. Anvil clouds above 10 km and middle-latitude storm track clouds in the winter hemisphere are observed to de-

TABLE 1. Global averages of the monthly averaged total, high-, middle-, and low-level cloud amounts simulated with EAULIQ and CONTROL, derived from the ISCCP-C2 dataset, for January and July. Units are in percent.

	EAULIQ	CONTROL	ISCCP-C2
	January		
Total cloud amount	71.5	79.3	62.7
High-level cloud amount	53.0	68.1	14.0
Mid-level cloud amount	30.7	19.6	19.2
Low-level cloud amount	33.2	27.3	24.9
	July		
Total cloud amount	69.4	78.6	62.9
High-level cloud amount	51.9	68.6	14.0
Mid-level cloud amount	29.6	16.6	17.0
Low-level cloud amount	29.1	23.4	26.2

crease and increase the most, respectively. Latitude–height cross sections of cloudiness for January reveal similar differences between EAULIQ and CONTROL (not shown).

The most obvious difference in C between EAULIQ and CONTROL is the significant decrease in high-level clouds, especially tropical upper-tropospheric clouds. Three factors contribute to this result. First, as shown in Fig. 3, EAULIQ leads to a significant decrease in cumulus incidence, which is in accordance with the decreased cumulus precipitation rate discussed in Part I. On a global average, the cumulus incidence decreases from 24.1% in CONTROL to 19.1% in EAULIQ in January and from 27.1% in CONTROL to 20.2% in EAULIQ in July. The decreased convective activity is linked to the decreased atmospheric radiative cooling between EAULIQ and CONTROL, which in turn results because of the decreased high-level cloudiness and the difference in the optical properties of anvil clouds between the two climate simulations, as will be discussed later. In EAULIQ, weaker convective detrainment produces smaller cloud water and cloud ice amounts, hence leading to lesser frequent occurrence of stratiform anvils. In contrast, strong convective activity leads to the formation of thick anvils in CONTROL.

A second factor is that the reduction in tropical anvil clouds partially results because the strong moistening of the tropical upper troposphere that occurs in CONTROL does not occur in EAULIQ (refer to Fig. 10 of Part I). As explained in Part I, in CONTROL, condensed water detrained at the tops of cumulus towers is assumed to immediately evaporate, hence enhancing the tropical upper-tropospheric relative humidity excessively, as discussed in section 5 of Part I. Cirrus clouds are predicted to form accordingly. In EAULIQ, condensed water detrained at the tops of cumulus towers is used as a source of cloud water and cloud ice in the cloud microphysics parameterization. No phase change takes place and the relative humidity does not vary as widely as in CONTROL. Comparing Fig. 5 of the present paper against Fig. 10 of Part I, it is obvious that the maximum in tropical upper-tropospheric clouds coincides with the maximum in the cumulus water vapor moistening rate in the CONTROL simulation.

The third part of the explanation is that the decrease in stratiform anvils at the tops of cumulus towers arises because, in EAULIQ, cloud water and cloud ice may immediately evaporate so that no clouds are predicted

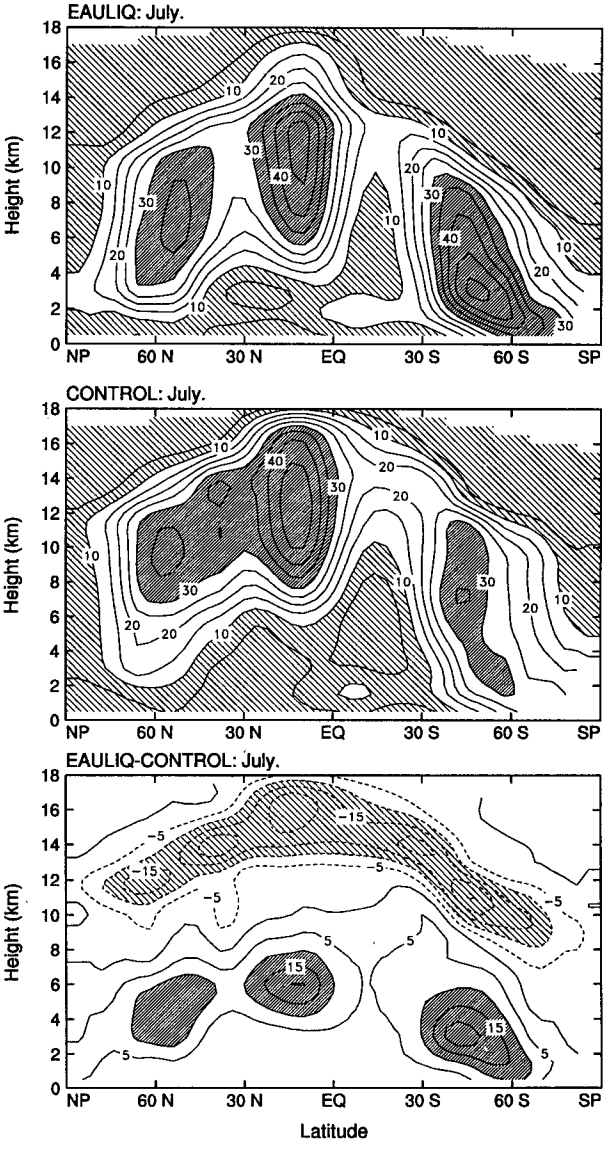

FIG. 5. Latitude–height cross sections of the monthly averaged cloud amount simulated with EAULIQ, CONTROL, and its difference EAULIQ minus CONTROL for July. Units are in percent and contour intervals are every 5%. Light shading corresponds to values less than 10% (less than −10% for the difference field), and heavy shading corresponds to values greater than 30% (greater than 10% for the difference field).

to form. This is not the case for CONTROL, for which convective anvils are assumed to form as soon as convective activity rises above 500 mb.

We now discuss the changes in cloud optical properties between EAULIQ and CONTROL. The latitude–height cross sections of the cloud optical depth (τ) obtained in both climate simulations and the difference between EAULIQ and CONTROL are displayed in Fig. 6 for July; τ is expressed as per millibar to eliminate its dependence on the thickness of the model layers.

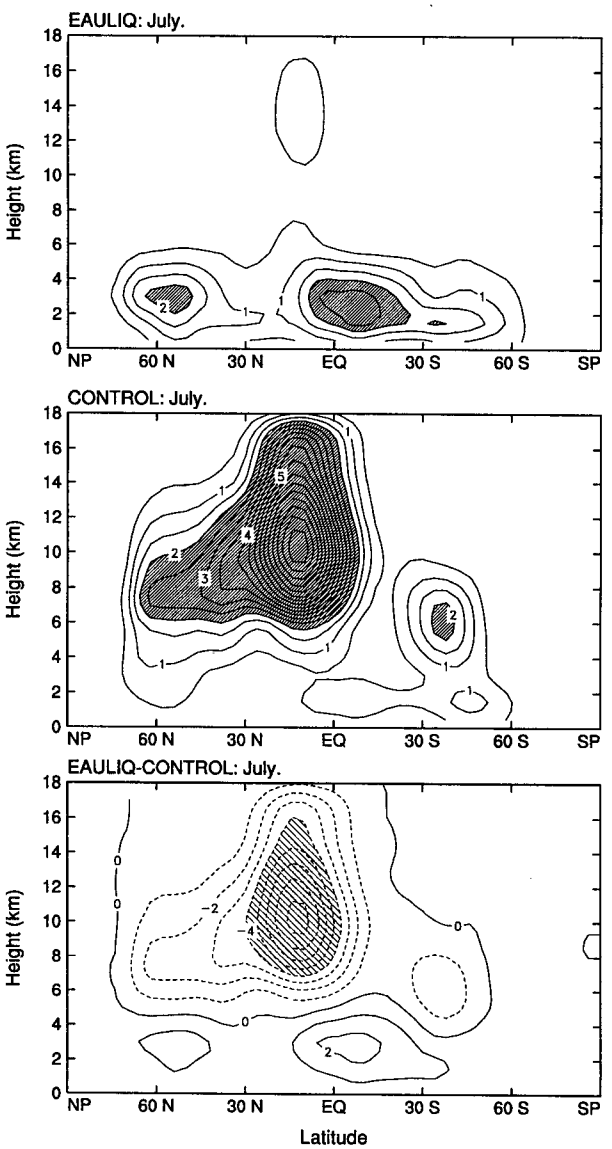

FIG. 6. Latitude–height cross sections of the monthly averaged cloud optical depth simulated with EAULIQ, CONTROL, and its difference EAULIQ minus CONTROL for July. Units are in 10^{-2} mb^{-1} and contour intervals are every 0.5 $\times$ 10^{-2} mb^{-1} (every 1 $\times$ 10^{-2} mb^{-1} for the difference field). Light shading corresponds to values less than -4×10^{-2} mb^{-1}, and heavy shading corresponds to values greater than 2×10^{-2} mb^{-1} (greater than 0 for the difference field).

The parameterization of the cloud optical properties as functions of the cloud water path instead of the mean cloud temperature, as well as the change in the distribution of C between EAULIQ and CONTROL, yields very large differences in the magnitude of τ between the two simulations. Variations in the vertical distribution of τ are due to variations in the vertical distribution of C, as discussed above. In EAULIQ, the optical thickness of tropical anvil clouds is strongly weakened whereas the optical thickness of the extratropical middle- and low-level clouds is enhanced, relative to CONTROL.

In CONTROL, we obtain values of τ in excess of 5 $\times$ 10^{-2} mb^{-1} for tropical anvil clouds because their cloud optical depth is assumed to be proportional to the pressure thickness of the clouds, following the parameterization of Harshvardhan et al. (1989). In contrast, τ for nonconvective clouds of the same pressure thickness would be smaller because, for those clouds, τ is assumed to rapidly decrease as cloud-top temperatures increase. The difference in the parameterization of τ between convective anvils and large-scale saturation clouds produces the very large difference in the latitudinal distribution of τ that is seen in Fig. 6.

In EAULIQ, the latitudinal difference in the magnitude of τ is not as dramatic as in CONTROL. The reason is that τ for tropical anvil clouds depends mainly on the cloud ice path, whereas τ for extratropical clouds depends mainly on the cloud water path since cloud water and cloud ice predominate in the middle latitudes and the Tropics, respectively (Part I). Greater cloud water paths and the small (10 μm) effective radius of cloud droplets versus smaller cloud ice paths and the large (30 μm) effective radius of cloud ice crystals, makes τ smaller in the Tropics than in middle latitudes. Although snow is the most abundant condensed water variable in EAULIQ (see Part I), its radiative effects are weak because the effective radius for snow is assumed to be 1000 μm. The change in ϵ between EAULIQ and CONTROL follows the same pattern as τ; it is omitted here for brevity. As for τ, the ϵ of tropical upper-tropospheric stratiform clouds simulated by EAULIQ is strongly reduced relative to CONTROL, whereas that of extratropical clouds is enhanced.

5. Cloud radiative forcing

a. Top-of-the-atmosphere cloud radiative forcing

The top-of-the-atmosphere radiative effect of clouds can be discussed in terms of the longwave (LWCRF) and shortwave (SWCRF) cloud radiative forcings. In view of the large differences in the distributions of cloudiness and its optical properties between EAULIQ and CONTROL, we expect to see significant variations in the distributions of LWCRF and SWCRF, and hence

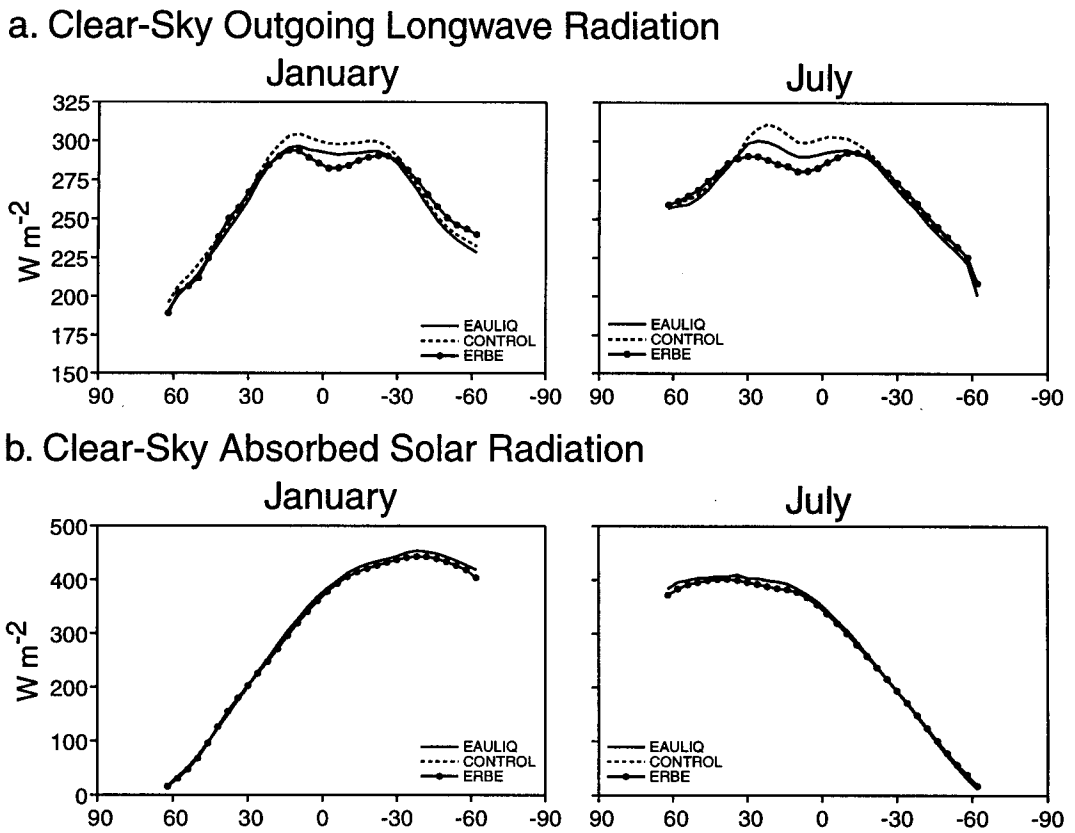

FIG. 7. Zonally averaged distributions of the monthly averaged (a) clear-sky outgoing longwave radiation and (b) clear-sky absorbed solar radiation simulated with EAULIQ and CONTROL and derived from the ERBE dataset between 60°N and 60°S for January and July. Units are in watts per square meter.

in the outgoing infrared radiation (OLR) and planetary albedo (α).

Following Ramanathan (1987), the cloud forcings at infrared and solar wavelengths are defined by

$$\text{LWCRF} = \text{OLR}_{cl} - \text{OLR} \tag{8}$$

and

$$\text{SWCRF} = -(\text{ABS}_{cl} - \text{ABS}), \tag{9}$$

where OLR_{cl} and ABS_{cl} are the clear-sky outgoing infrared radiation and clear-sky absorbed solar radiation. By subtracting the clear-sky components of the planetary radiation budget, we separate the effects of clouds from the radiative effects of the earth's surface and the gaseous atmosphere. In evaluating the model's ability to simulate the radiative effects of clouds by comparison with satellite-derived estimates, it is important to remember that the accuracy with which LWCRF and SWCRF can be determined from space depends strongly on the determination of OLR_{cl} and ABS_{cl}, which is most difficult for overcast regions where LWCRF and SWCRF are the largest. In ERBE, the retrievals of OLR_{cl} and ABS_{cl}, and then of LWCRF and SWCRF, are mainly based upon a threshold discrimination of the longwave and shortwave radiation fluxes between clear-sky and cloudy pixels (Ramanathan 1987). With the CSU GCM, OLR_{cl} and ABS_{cl} are computed using the same atmospheric profiles as the cloudy outgoing longwave radiation and absorbed solar radiation but for clear-sky conditions (Method 2 of Cess and Potter 1987).

Before comparing the simulations of LWCRF and SWCRF with satellite observations, we compare the zonally averaged profiles of OLR_{cl} and ABS_{cl}, as simulated by EAULIQ and CONTROL against ERBE data, for January and July. Figure 7 indicates that both EAULIQ and CONTROL satisfactorily reproduce the zonally averaged OLR_{cl} in the middle and high latitudes but systematically overestimate OLR_{cl} between 30°N and 30°S in both months, especially in July. In the Tropics, the difference between the model and satellite data reaches values in the order of 25 W m^{-2} in CONTROL and 10 W m^{-2} in EAULIQ. Differences between the simulated and observed OLR_{cl} in the Tropics arise from several causes. One is that the simulated atmosphere is too dry (refer to Fig. 12 of Part I) and too warm around the tropical tropopause, as will be discussed later in section 6. Both EAULIQ and CON-

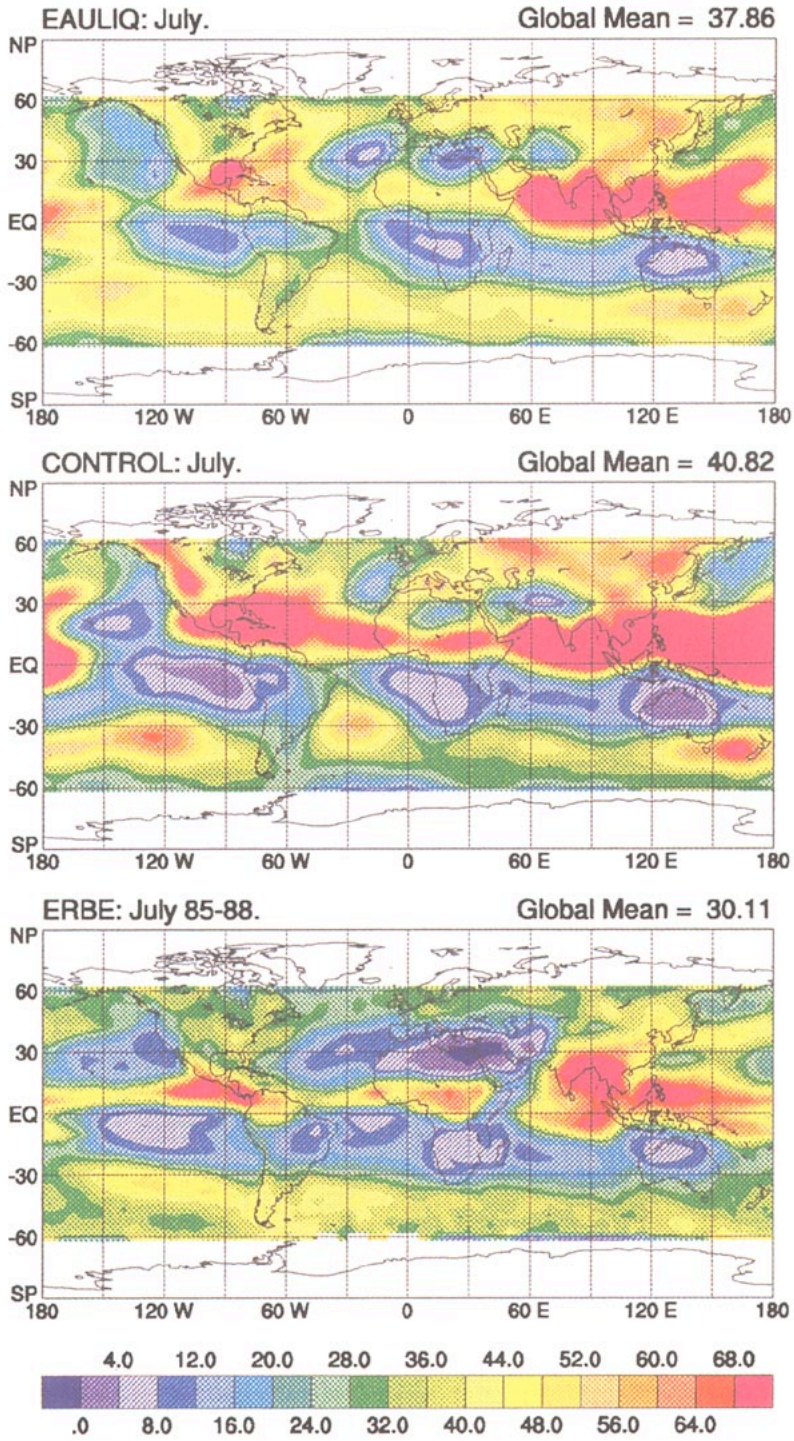

FIG. 8. Geographical distributions of the monthly averaged longwave cloud radiative forcing simulated with EAULIQ, CONTROL, and derived from the ERBE dataset between 60°N and 60°S for July. Units are in watts per square meter.

TROL overestimate the clear-sky absorption of solar radiation in the summer hemisphere.

In Fig. 8, we compare the global maps of the monthly averaged LWCRF obtained with EAULIQ and CONTROL against that derived from ERBE scanner data for July. Figure 9 shows global maps of the difference in the monthly averaged LWCRF between January and July, as simulated with EAULIQ and CONTROL and

from satellite data. Finally, Fig. 10 shows the zonally averaged distributions of LWCRF and OLR simulated with EAULIQ and CONTROL against ERBE data for January and July. Global maps of the monthly averaged SWCRF are shown in Fig. 11, whereas Fig. 12 displays the quantity $\bar{S}\Delta\alpha$ to illustrate the change in the monthly averaged SWCRF between January and July, as simulated with EAULIQ and CONTROL, against ERBE data. Here $\bar{S}$ is the top-of-the-atmosphere averaged shortwave incident radiation between January and July, and $\Delta\alpha$ is the difference in α between the two months. Finally, Fig. 13 displays the zonally averaged profiles of SWCRF and α. January and July maps of OLR and α are omitted here for brevity. Global averages of the various longwave and shortwave radiation components are listed in Table 2.

Satellite observations show that LWCRF is positive everywhere, indicating that the longwave radiative effect of clouds is to reduce the emission of the earth–atmosphere system. ERBE scanner data indicate that LWCRF is strongest above the deep tropical convective regions in July, that is, Central America, equatorial Africa, Southeast Asia, and the tropical Western Pacific. Also LWCRF is large above the storm track regions over the Southern Ocean. In these regions, cold cloud-top stratiform anvils are very efficient at reducing the top-of-the-atmosphere longwave radiative cooling. High-level clouds "trap" outgoing infrared radiation at their bases, hence enhancing the warming of the atmosphere and the earth's surface, while emitting infrared radiation at much colder cloud-top temperatures. The greenhouse effect of the clouds is directly related to the temperature difference between the cloud top and surface and to the amount of water vapor. Tropical clouds and associated cloud anvils are more efficient at warming the atmosphere and the earth's surface than middle-latitude frontal clouds. Outside these regions, LWCRF is small.

Differences in LWCRF between CONTROL and ERBE are quite large. As seen in Fig. 10, CONTROL overestimates the intensity of the zonally averaged LWCRF in the Tropics by as much as 30 W m^{-2} at the equator and in the middle latitudes of the summer hemisphere, especially in July. At regional scales, the discrepancy in LWCRF between CONTROL and ERBE across Central America, equatorial Africa, the Western Pacific and Indian Oceans is very striking. Over these regions, Fig. 8 indicates a difference in excess of 25 W m^{-2} between the model and the satellite data.

When compared with satellite data, EAULIQ gives a significant improvement in the simulated LWCRF relative to CONTROL, especially in the Tropics. The reasons are that EAULIQ produces optically thinner high-level clouds, and also cumulus convective activity is significantly decreased, as shown in Fig. 3. Figure 10 indicates that EAULIQ yields a strong decrease in the zonally averaged LWCRF between 30°N and 30°S but does not perform as well as CONTROL at poleward latitudes, especially in the subtropics. At regional scales, there is a significant improvement in the simulated LWCRF over the western Pacific and Indian Oceans, although it is still overestimated. Also the LWCRF maximum simulated by CONTROL over Central America is reduced. However, the LWCRF simulated with EAULIQ remains too strong over the Southern Oceans in July when compared against satellite data.

Figure 9 indicates that EAULIQ leads to a significant improvement in the simulation of the seasonal cycle of LWCRF relative to CONTROL when compared with ERBE data. As for the seasonal cycle of C, the difference in LWCRF between January and July over the tropical convective regions is much better simulated in EAULIQ than in CONTROL, especially over the Western Pacific and Indian Oceans. In EAULIQ, the strength of the seasonal cycle is also strongly reduced at low latitudes. However, EAULIQ overestimates the seasonal cycle in LWCRF in the middle latitudes of both hemispheres when compared against satellite data.

EAULIQ yields an improved simulation of the minimum OLR in the Tropics but systematically underestimates its magnitude outside of the Tropics, especially in the subtropics. At equatorial latitudes, the OLR minimum in EAULIQ is not as low as that of CONTROL, and this is consistent with the decreased LWCRF obtained in EAULIQ over the tropical convective regions, especially over the monsoon areas. In the subtropics, as in the middle latitudes, the OLR of EAULIQ is colder than that of CONTROL and is too low compared with ERBE data, especially in January. Since EAULIQ satisfactorily simulates the zonal OLR_{cl} poleward of 30°N and 30°S (refer to Fig. 7), the underestimation of the simulated OLR is then due to the fact that EAULIQ overestimates the total cloud amount at these latitudes, as shown in Fig. 3. In CONTROL, the overestimation of OLR relative to EAULIQ and ERBE at subtropical latitudes in the winter hemisphere may result because the simulated OLR_{cl} is too warm, as shown in Fig. 7, and arises despite that the simulated total cloud amount is greater than those simulated in EAULIQ and obtained from ISCCP-C2 data. Table 2 indicates that, on a global average, EAULIQ and CONTROL underestimate the OLR by -5.4 and -1.8 W m^{-2} in January and -6.2 and -3.4 W m^{-2} in July, respectively.

As for LWCRF, the differences in SWCRF between CONTROL and ERBE are quite important. CONTROL strongly overestimates SWCRF over the tropical convective regions, especially over the western Pacific and Indian Oceans, as well as over the continents of the summer hemisphere. Figure 13 indicates that the difference in the zonally averaged SWCRF between CONTROL and ERBE exceeds 50 W m^{-2} in the Tropics but rapidly decreases at higher latitudes. As shown in Fig. 11, EAULIQ yields some improvement in the simulated SWCRF, especially over the western Pacific and Indian Oceans in July. Over the monsoon areas,

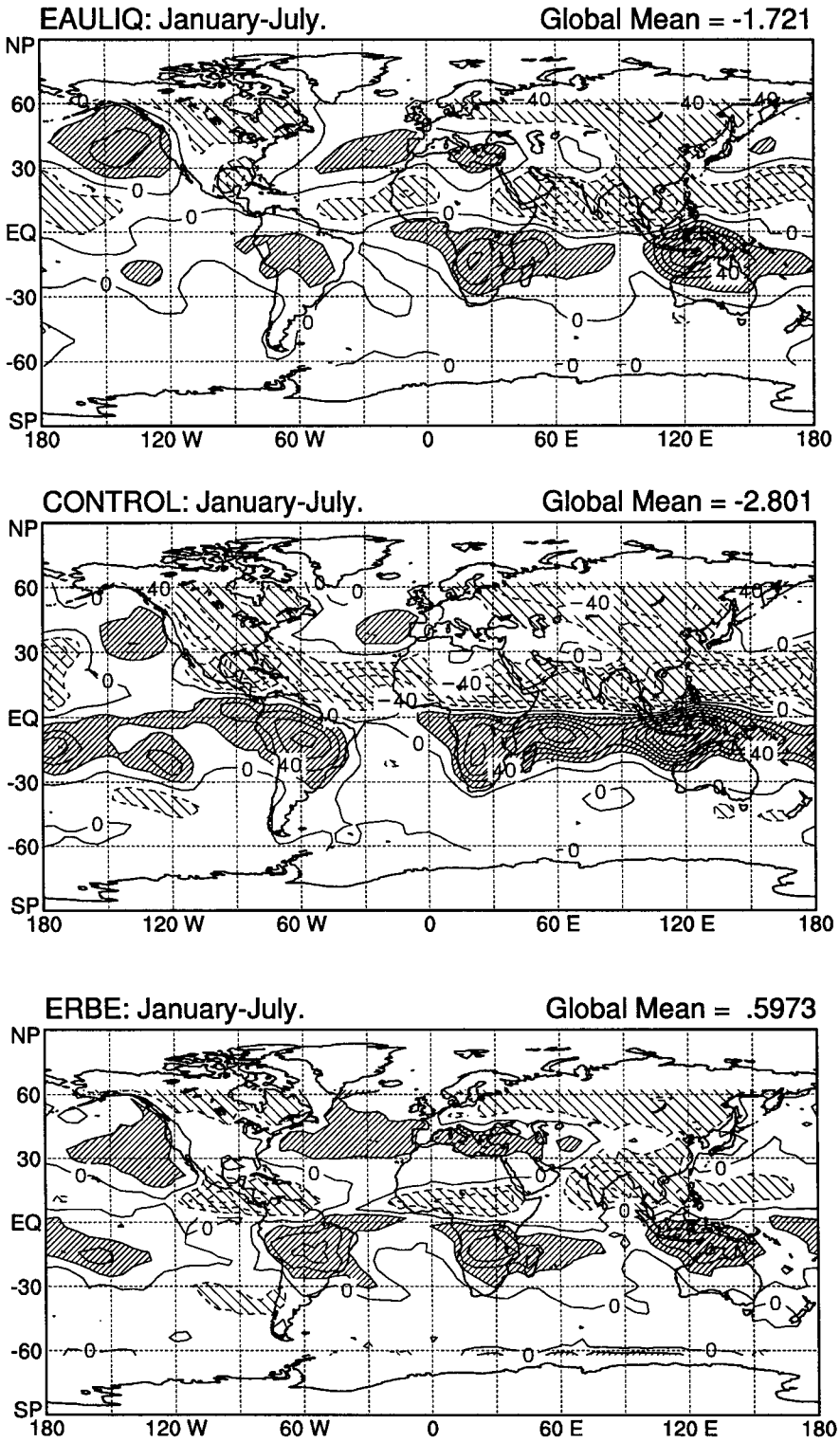

FIG. 9. Geographical distributions of the difference January minus July in the monthly averaged longwave cloud radiative forcing simulated with EAULIQ, CONTROL, and obtained from the ERBE dataset between 60°N and 60°S. Units are in watts per square meter and contour intervals are every 10 W m^{-2}. Light shading corresponds to values less than -10 W m^{-2} and heavy shading corresponds to values greater than 10 W m^{-2}.

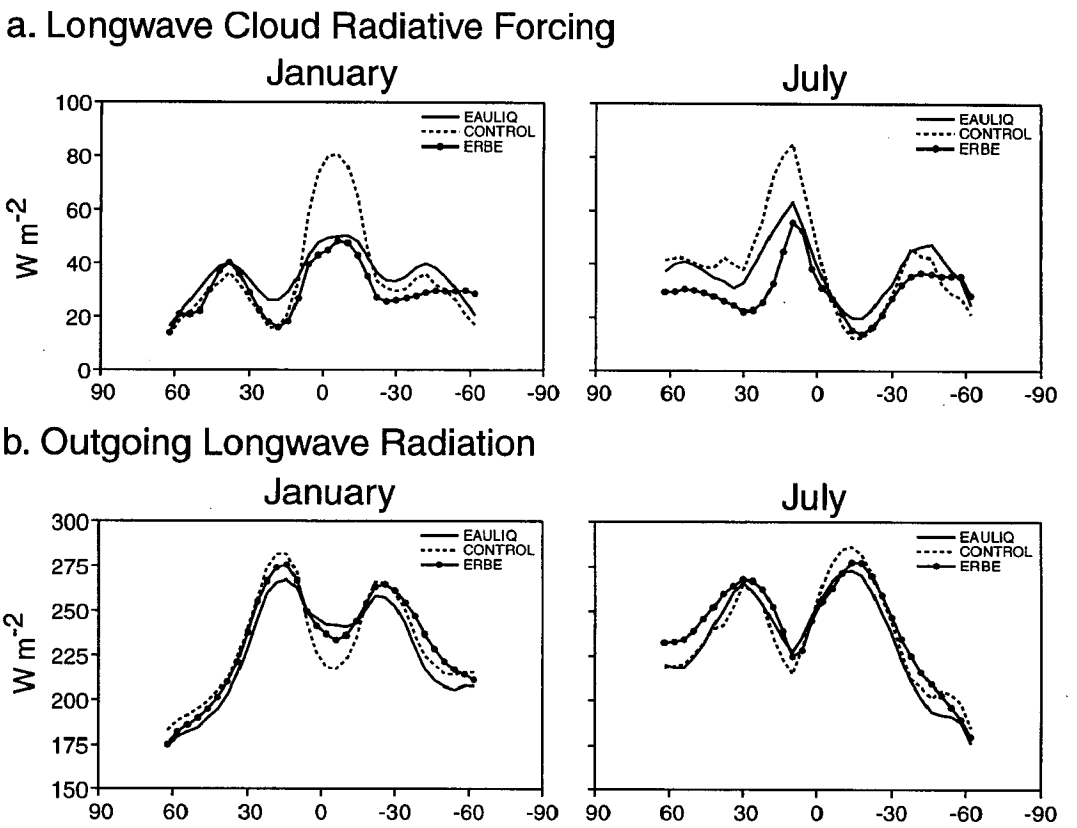

FIG. 10. Zonally averaged distributions of the monthly averaged (a) longwave cloud radiative forcing and (b) outgoing longwave radiation simulated with EAULIQ and CONTROL and derived from the ERBE dataset between 60°N and 60°S for January and July. Units are in watts per square meter.

SWCRF increases from values in excess of -140 W m^{-2} in CONTROL to values less than -120 W m^{-2}, compared to -80 W m^{-2} in ERBE. As shown in Fig. 13, EAULIQ overestimates the magnitude of SWCRF outside of the Tropics, which leads to a globally averaged value of SWCRF that is 13.7 W m^{-2} and 13.4 W m^{-2} greater than that from ERBE data in January and July, respectively. Figure 12 shows that, as for LWCRF, the seasonal cycle of SWCRF is significantly improved between EAULIQ and CONTROL over the tropical convective regions. Its intensity is much weaker than that in CONTROL over the western Pacific and Indian Oceans. As for LWCRF, EAULIQ has a tendency to overestimate SWCRF over the middle latitude storm track regions.

As seen in Fig. 13, CONTROL yields zonally averaged values of α that are unrealistically high along the ITCZ but in satisfactory agreement against ERBE data poleward of 30°N and 30°S. On a zonal average, the difference between model and observations exceeds 10% in the Tropics. This is not surprising considering the magnitude of τ shown in Fig. 6. When compared against CONTROL and ERBE data, EAULIQ yields a slight reduction in the zonal α in the Tropics but strongly overestimates its magnitude outside of the Tropics, especially in the winter hemisphere. Difference maps of α between EAULIQ and CONTROL show that EAULIQ leads to a decrease in α over the deep convective regions, especially over the western Pacific Ocean and the monsoon regions and an increase in α relative to CONTROL over the rest of the globe. This result is in accordance with the change in SWCRF between the two simulations. We conclude that the parameterization of τ as a function of the cloud water, cloud ice, and snow path used in EAULIQ yields more realistic results than that used in CONTROL over deep convective regions, but fails to satisfactorily simulate shortwave characteristics of the planetary radiation budget outside of the Tropics.

In summary, changing the parameterization of the prediction of cloud formation and the optical properties of cloudiness yields a significant improvement in the geographical distribution and intensity of the simulated longwave and shortwave cloud radiative forcings between EAULIQ and CONTROL relative to ERBE data over deep tropical convective activity regions. In EAULIQ, the simulation of the

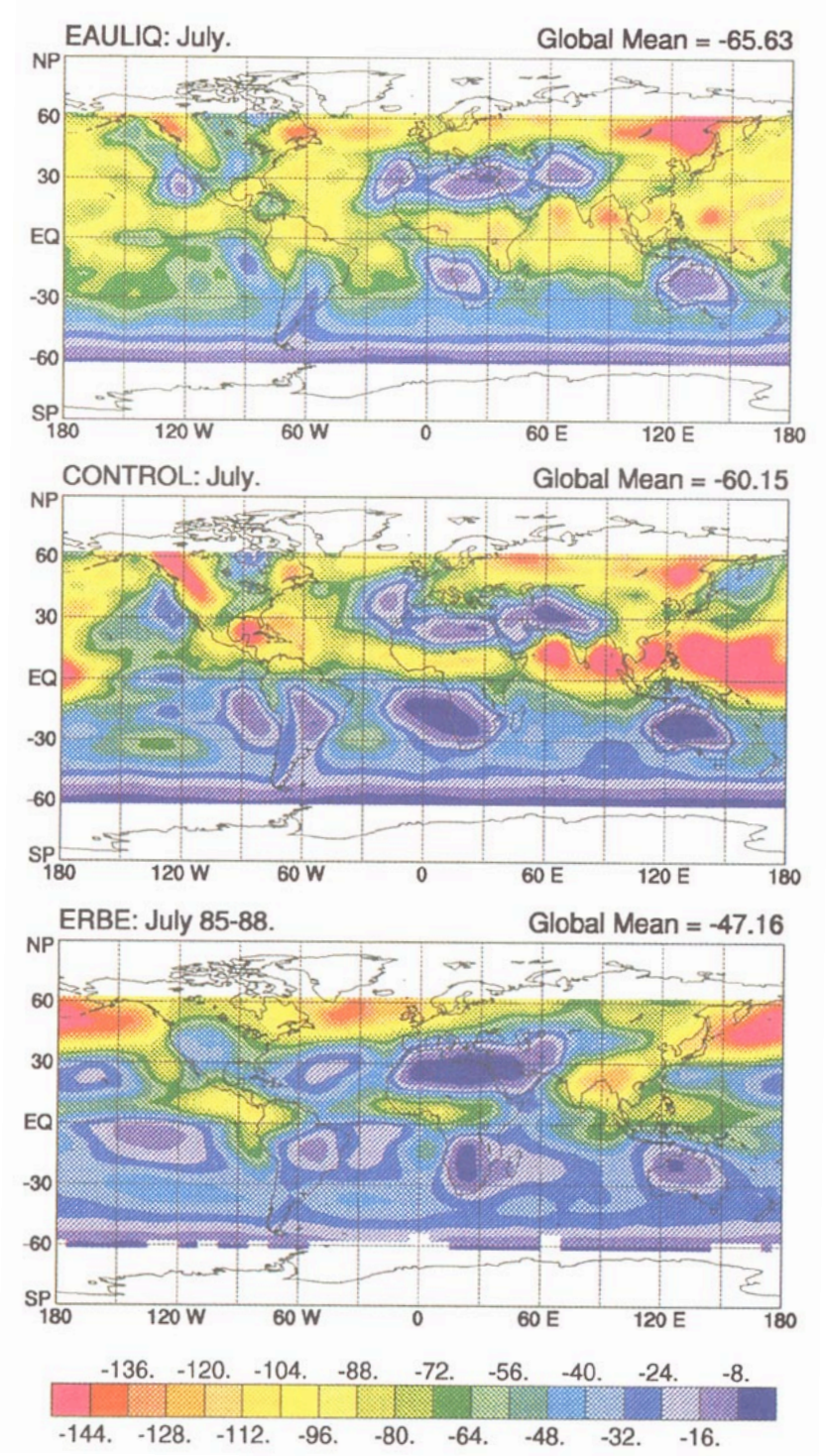

FIG. 11. Geographical distributions of the monthly averaged shortwave cloud radiative forcing simulated with EAULIQ and CONTROL and derived from the ERBE dataset between 60°N and 60°S for July. Units are in watts per square meter.

planetary radiation budget is not as satisfactory as in CONTROL outside of the Tropics. In the Tropics, the change in the simulated forcings is mainly due to the reduced occurrence of stratiform anvils, and also that the stratiform anvils are optically thinner in EAULIQ than in CONTROL.

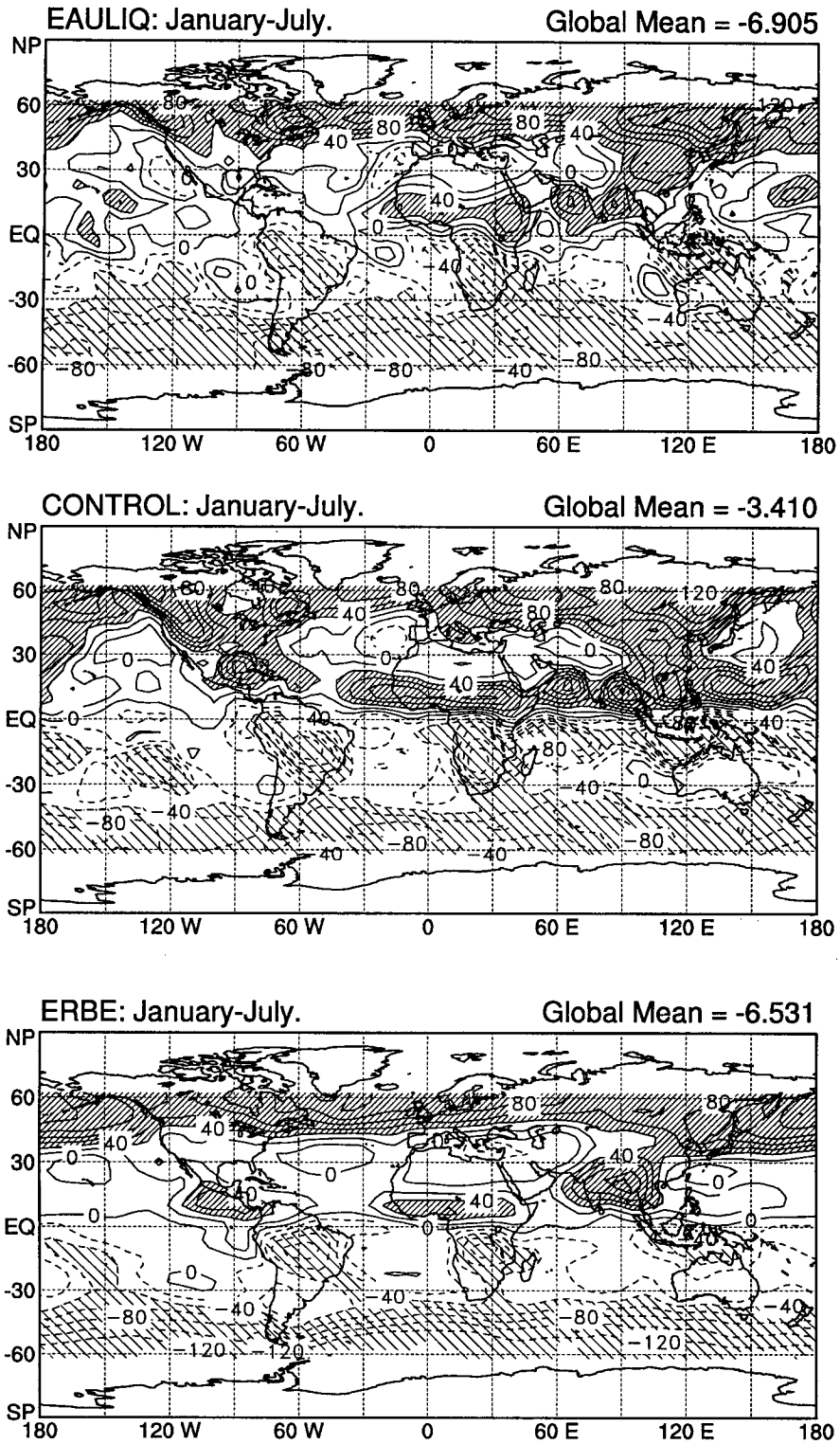

FIG. 12. Geographical distributions of the difference January minus July in the monthly averaged shortwave cloud radiative forcing simulated with EAULIQ and CONTROL and obtained from the ERBE dataset between 60°N and 60°S. Units are in watts per square meter and contour intervals are every 20 W m^{-2}. Light shading corresponds to values less than −40 W m^{-2}, and heavy shading corresponds to values greater than 40 W m^{-2}.

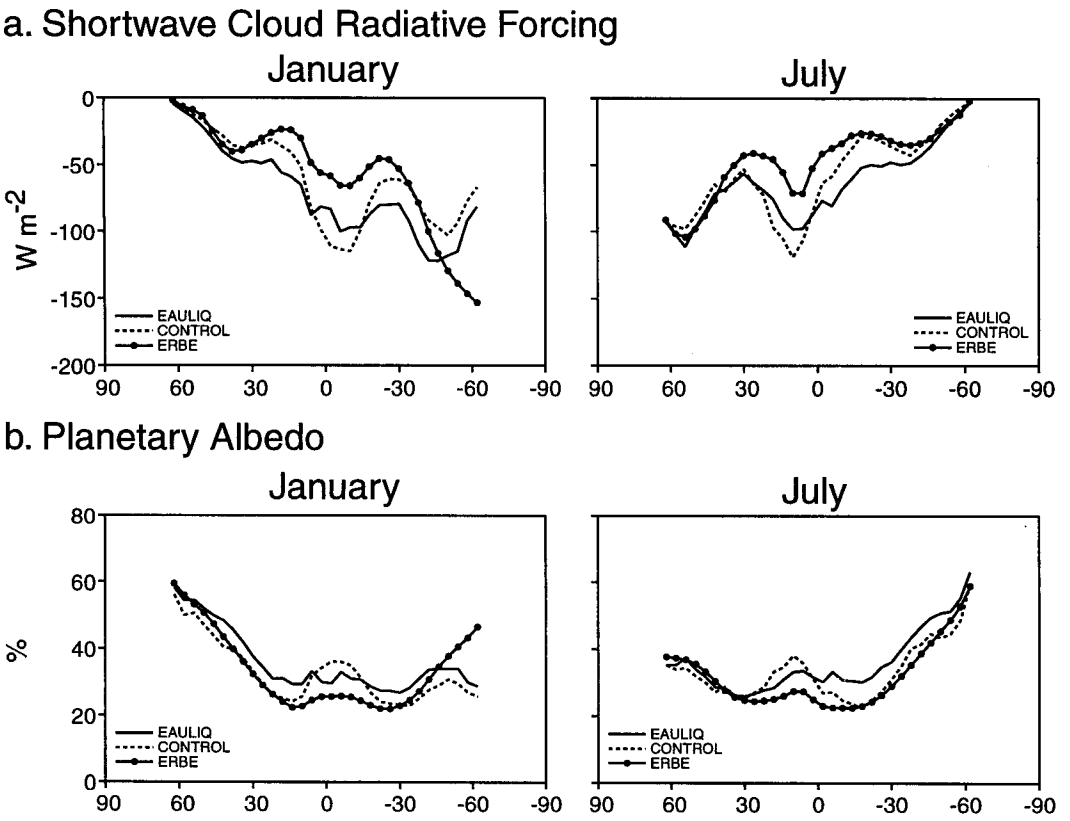

FIG. 13. Zonally averaged distributions of the monthly averaged (a) shortwave cloud radiative forcing and (b) planetary albedo simulated with EAULIQ and CONTROL and derived from the ERBE dataset between 60°N and 60°S for January and July. Units are in watts per square meter in (a) and in percent in (b).

b. Surface radiation

Before examining the geographical distribution of the atmospheric radiative cooling, we briefly discussed the difference in the surface radiation budget between EAULIQ and CONTROL.

Figures 14 and 15 show the zonally averaged distributions of the surface net longwave and surface net shortwave radiation for clear-sky and all-sky conditions. In Fig. 14, we have also plotted the surface net longwave radiation estimates of Gupta et al. (1993), and in Fig. 15 we show the surface net shortwave radiation data of Li and Leighton (1993). Gupta et al. derived global surface and atmospheric radiation components using parameterized radiation models with satellite meteorological data from ISCCP and directly measured top-of-the-atmosphere radiative fluxes from ERBE. Li and Leighton used a linear relationship between the top-of-the-atmosphere reflected flux and the flux absorbed at the surface for a fixed solar zenith angle. Because global surface longwave and shortwave radiation fields cannot be measured from space, they are not direct observations and hence should be used with caution.

Figure 14 shows that EAULIQ and CONTROL overestimate the zonal clear-sky surface net longwave radiation relative to the data of Gupta et al. (1993) at almost all latitudes in both months except in the subtropics of the winter hemisphere. Both EAULIQ and CONTROL also strongly overestimate the magnitude of the zonal surface net longwave radiation at all latitudes. Figure 15 indicates that both EAULIQ and CONTROL overestimate the clear-sky shortwave net radiation flux in the summer hemisphere by as much as 50 W m^{-2} in the zonal average. This large error is common to existing GCMs (Garratt et al. 1993; Garratt 1994). It may be due to neglect of aerosols and trace gases. For the zonal distribution of the surface net shortwave radiation, CONTROL and EAULIQ produce a very good agreement against the data of Li and Leighton up to 30° of latitude in the summer hemisphere.

c. Atmospheric radiative cooling

In Part I, we showed that cumulus precipitation was strongly reduced in EAULIQ relative to CONTROL (in a global average, by -0.6 mm day^{-1} in January and

TABLE 2. Global averages of the monthly averaged components of the planetary radiation budget simulated with EAULIQ and CONTROL and derived from the ERBE dataset for January and July.

	EAULIQ	CONTROL	ERBE
	January		
Outgoing infrared radiation (W m^{-2})	227.0	230.6	232.4
Planetary albedo (%)	33.3	31.0	30.8
Absorbed shortwave radiation (W m^{-2})	234.9	243.3	248.0
Clear-sky outgoing longwave radiation (W m^{-2})	260.9	266.0	261.3
Clear-sky absorbed shortwave radiation (W m^{-2})	301.6	301.6	301.4
Longwave cloud radiative forcing (W m^{-2})	33.9	35.3	28.7
Shortwave cloud radiative forcing (W m^{-2})	−66.7	−58.3	−53.0
	July		
Outgoing infrared radiation (W m^{-2})	233.0	235.8	239.2
Planetary albedo (%)	33.0	31.4	29.1
Absorbed shortwave radiation (W m^{-2})	221.5	226.8	243.0
Clear-sky outgoing longwave radiation (W m^{-2})	268.4	273.7	267.7
Clear-sky absorbed shortwave radiation (W m^{-2})	283.1	283.0	294.4
Longwave cloud radiative forcing (W m^{-2})	35.5	37.9	28.3
Shortwave cloud radiative forcing (W m^{-2})	−61.6	−56.2	−48.2

−0.7 mm day^{-1} in July) and that cumulus convection did not penetrate as high in EAULIQ as in CONTROL. We explained this difference in terms of an increased static stability of the atmosphere due to a decrease in the atmospheric radiative cooling (ARC) between EAULIQ and CONTROL. Here the ARC is defined as the difference between the surface and top-of-the-atmosphere net (longwave and shortwave) radiation. It is defined so that positive values indicate atmospheric radiative cooling. Figure 16 shows the zonally averaged distributions of the ARC and its longwave and shortwave components simulated by EAULIQ and CONTROL for January and July. The zonally averaged temperature lapse rate (Γ) is displayed in Fig. 17, also for both months. In Fig. 17, Γ was obtained by computing the difference between the temperature at 300 mb and that of the surface divided by the 300-mb height above the surface.

As seen in Fig. 16, the longwave component of the ARC dominates the total ARC since the top-of-the-atmosphere shortwave absorption is small, especially in the winter hemisphere. Maps of the ARC would show that the maximum ARC is located over the mostly cloud-free subtropical latitudes, especially over the oceans, whereas the minimum ARC is found over the tropical convectively active regions. Of course, there is a close correspondence between the geographical distribution of the cloudy component of the ARC and the radiative forcing of clouds, especially at long wavelengths. Areas of large ARC correspond to areas of small LWCRF, and vice versa, areas of small ARC correspond to areas of large LWCRF. Figure 16 shows that the two runs give generally similar results, but CONTROL has stronger gradients, especially in the Tropics. ARC gradients will tend to drive vertical motion gradients, so this is an indication that the CONTROL will be more dynamically active than EAULIQ, especially in the Tropics; this is, in fact, true. The zonal ARC slightly decreases between EAULIQ and CONTROL in the winter hemisphere, especially at subtropical latitudes, whereas it increases along the ITCZ. In the subtropics, the difference between EAULIQ and CONTROL results because the subtropical oceans are slightly more cloudy in EAULIQ than in CONTROL, as also seen in Fig. 8. At equatorial latitudes, the increase in the ARC is due to the amount of high-level clouds and convective activity reduced between the two simulations, as explained earlier.

As shown in Fig. 17, the change in the ARC between EAULIQ and CONTROL leads to an increased static stability of the atmosphere between the two simulations. On a zonal average, Γ decreases by about 0.25 K day^{-1} between 30°N and 60°S in January and between 30°S and 60°N in July. By looking at global maps (not shown here), it can be seen that the change in Γ is weaker in the Tropics than in the middle latitudes, indicating nevertheless an increased static stability of the tropical atmosphere in EAULIQ. The difference in the ARC between EAULIQ and CONTROL is best explained when looking at Figs. 18 and 19. Figure 18 displays the latitude–height cross sections of the longwave and shortwave radiative heating rates, whereas Fig. 19 shows the latitude–height cross section of the net radiative rate simulated with both runs, also for July.

As shown in Fig. 5, tropical upper-tropospheric clouds are less abundant, have a smaller cloud infrared emissivity, and occur at lower levels in EAULIQ relative to CONTROL. As a result, the strong longwave radiative cooling due to tropical anvils that occurs at the 16-km level in CONTROL is significantly decreased in EAULIQ. In contrast, the difference in the longwave radiative cooling between EAULIQ and CONTROL is positive at about 8 km due to the lower altitude of stratiform anvils produced by EAULIQ. The dipole structure that is seen in the difference in the tropical longwave radiative cooling between EAULIQ and CONTROL results because tropical stratiform anvils are not predicted to form as high and are not as optically thick in EAULIQ as in CONTROL. This is not true for lower tropical and extratropical stratiform clouds that exhibit a stronger longwave radiative cooling in EAULIQ than in CONTROL, as shown in Fig.

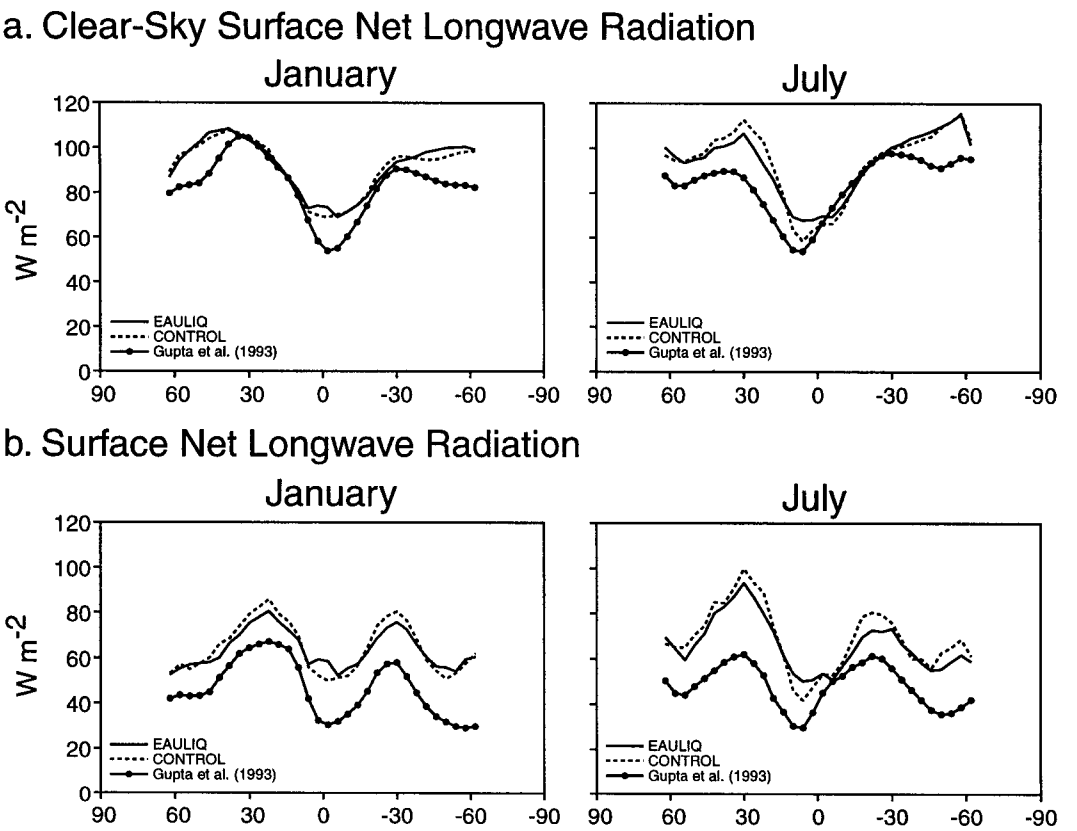

FIG. 14. Zonally averaged distributions of the monthly averaged (a) clear-sky surface net longwave radiation and (b) surface net longwave radiation simulated with EAULIQ and CONTROL and estimated by Gupta et al. (1993) between 60°N and 60°S for January and July. Units are in watts per square meter.

18. This result is in accordance with Fig. 5, which indicates that middle tropospheric clouds are more abundant in EAULIQ than in CONTROL, hence enhancing the radiative cooling of the middle troposphere between 60°N and 60°S. As shown in Fig. 18, the decrease in the optical thickness of tropical and extratropical stratiform anvils between EAULIQ and CONTROL leads to a reduced shortwave radiative heating of the upper troposphere, especially in the summer hemisphere. In summary, as seen in Fig. 19, the decrease in the amount and optical thickness of upper-tropospheric clouds leads to an increased radiative heating of the upper troposphere in both hemispheres. The decrease in the cloud-top height of tropical stratiform anvils produce a decreased radiative heating of the middle troposphere along the ITCZ.

The decrease in the ARC and Γ that occurs in EAULIQ relative to CONTROL can partly explain the decrease in the cumulus and total precipitation rates, discussed in Part I. On a global average, the atmospheric radiative cooling must balance the sum of the latent and sensible heat fluxes. Because the globally averaged sensible heat flux is much smaller than the latent heat flux, most of the variations in the ARC will affect the latent heat flux, and so precipitation. Although this relationship does not hold at regional scales, it is important to note the strong correlation between the increased ARC and the decreased cumulus precipitation in the Tropics, as shown in Fig. 16 here and Fig. 16 of Part I.

Figure 20 shows joint probability functions (PDFs) for the ARC and the latent heat of condensation times the precipitation rate for both EAULIQ and CONTROL. The input data are monthly means of the respective quantities at each grid point. In computing the PDFs, the areas of the grid cells are taken into account. The CONTROL run has a broader range of values for both the ARC and the latent heating rate.

Both runs show two well separated branches: a "lower" one with high precipitation rates and an ARC that is weak and a stronger, more concentrated "upper" branch with larger values of the ARC. The lower branches correspond to the summer hemisphere and the cloudy regions of the Tropics, in each run, while the upper branches correspond to the winter hemisphere. There is a maximum of the PDF along a "ridge" that runs through the upper branch, jutting out from lower left to lower right. Along this ridge, the ARC and the

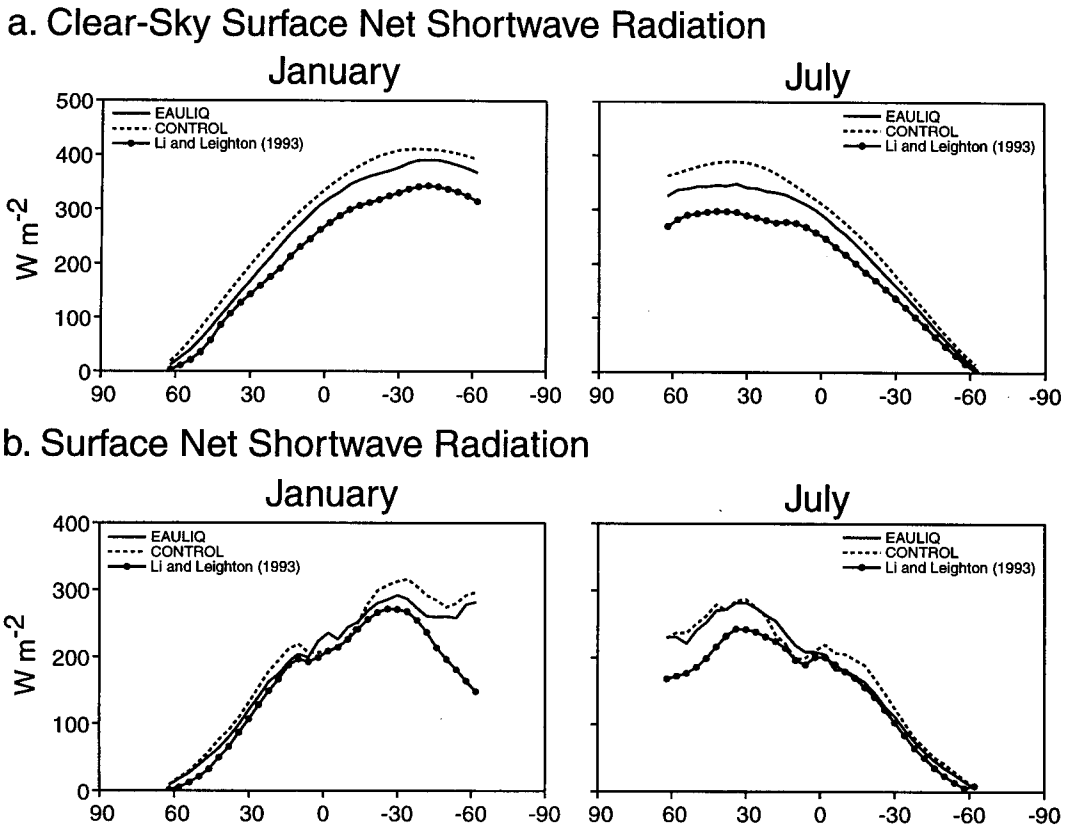

FIG. 15. Zonally averaged distributions of the monthly averaged (a) clear-sky surface net shortwave radiation and (b) surface net shortwave radiation simulated by EAULIQ and CONTROL, estimated by Li and Leighton (1993) between 60°N and 60°S for January and July. Units are in watts per square meter.

latent heating rate increase together, although at different rates.

Where the precipitation rate is very large, on the right sides of the diagrams, there is a tendency for the ARC to become weaker as the precipitation rate becomes stronger; the PDF slopes from upper left to lower right. An interpretation is that stronger precipitation is accompanied with more high cloudiness, which tends to reduce the ARC. As already discussed, just the opposite effect must occur globally because globally the ARC is balanced mainly by latent heat release so that the two must increase or decrease together.

6. Atmospheric general circulation

We now compare a few components of the atmospheric general circulation as simulated in EAULIQ and CONTROL.

Differences in the vertical distributions of the temperature and zonal wind component simulated by EAULIQ and CONTROL essentially result from differences in the distributions of the radiative and latent heatings. Figures 21 and 22 show latitude–height cross sections of the temperature and zonal wind components simulated by EAULIQ and CONTROL and obtained from ECMWF data, as well as the differences EAULIQ minus ECMWF, CONTROL minus ECMWF, and EAULIQ minus CONTROL for July. Corresponding January latitude–height cross sections are omitted here for brevity. Figure 23 shows the latitude–height cross sections of the latent heating and the sum of the net radiative heating and latent heating, also for July. We refer to that sum as simply the total diabatic heating although it does not include heating due to dry convective adjustment and any heating occurring in the PBL. In Fig. 23, the latent heating rate is the sum of the heating rates due to cumulus convection (Arakawa and Schubert 1974), moist convective adjustment (Manabe et al. 1965) used to represent convection originating above the PBL, and stratiform condensation (Part I).

Comparisons between the temperature simulated by EAULIQ and CONTROL against that obtained from ECMWF data indicate that the simulated upper-troposphere and stratosphere are systematically too cold and

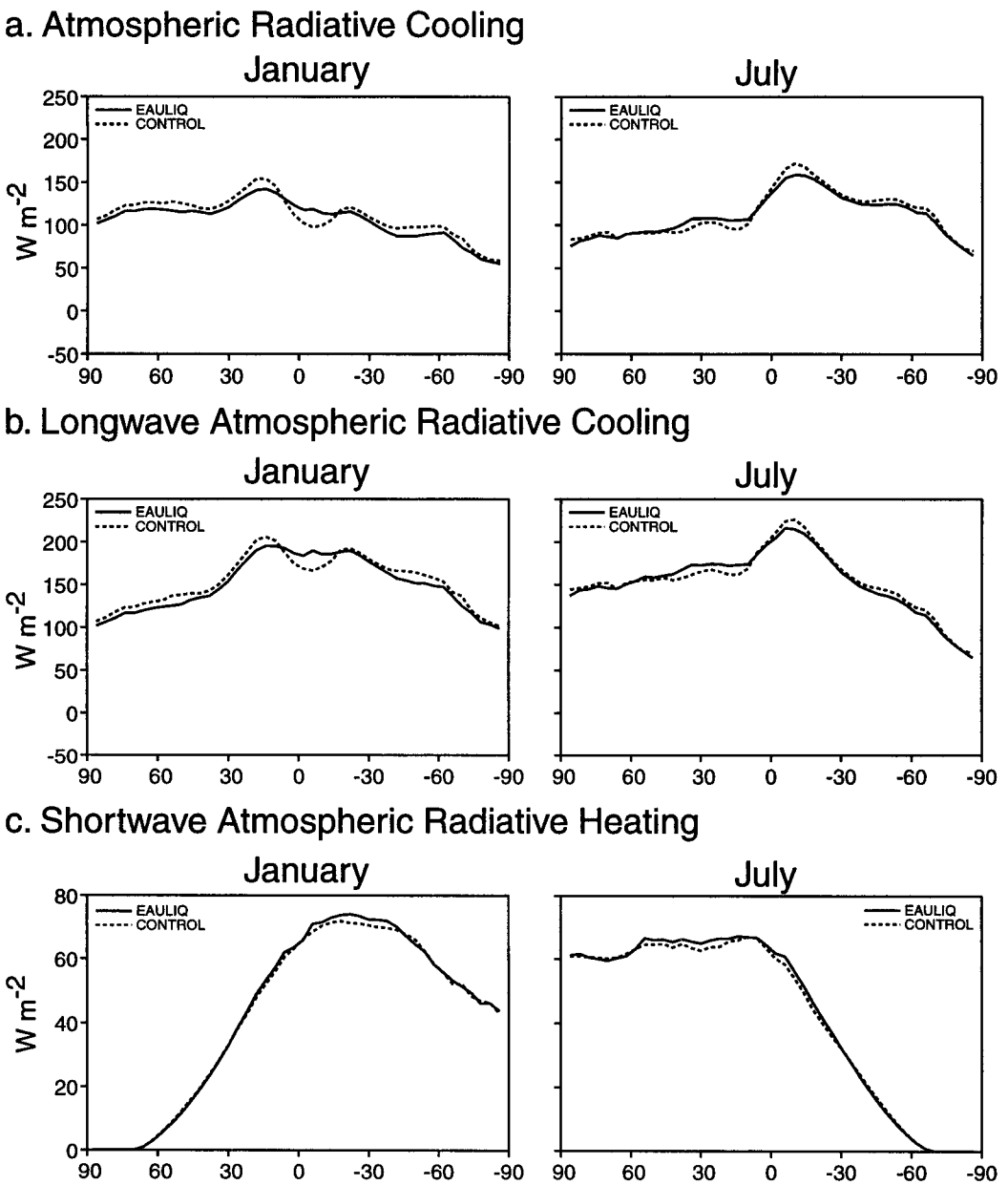

FIG. 16. Zonally averaged distributions of (a) the atmospheric radiative cooling, (b) the longwave atmospheric radiative cooling, and (c) the shortwave atmospheric radiative heating simulated by EAULIQ and CONTROL. Units are in watts per square meter.

the simulated troposphere systematically too warm when compared against observations. In the Tropics, the maximum in the warm bias shifts from the low troposphere in CONTROL to the upper troposphere in EAULIQ. The temperature difference between EAULIQ and CONTROL shows that the troposphere is warmer in EAULIQ than in CONTROL except at low altitudes in the Tropics. The temperature difference between the two simulations exceeds 5 K in the upper troposphere in the summer hemisphere, while it is less than −3 K in the low tropical troposphere. Also EAULIQ yields a colder upper troposphere and stratosphere in the winter hemisphere when compared against CONTROL.

As seen in Fig. 22 and in accordance with the difference in the meridional temperature gradient between EAULIQ, CONTROL, and ECMWF observations, EAULIQ and CONTROL yield an unrealistically strong westerly jet in the winter hemisphere and a subtropical jet in the summer hemisphere. The difference between the simulated and observed zonal winds

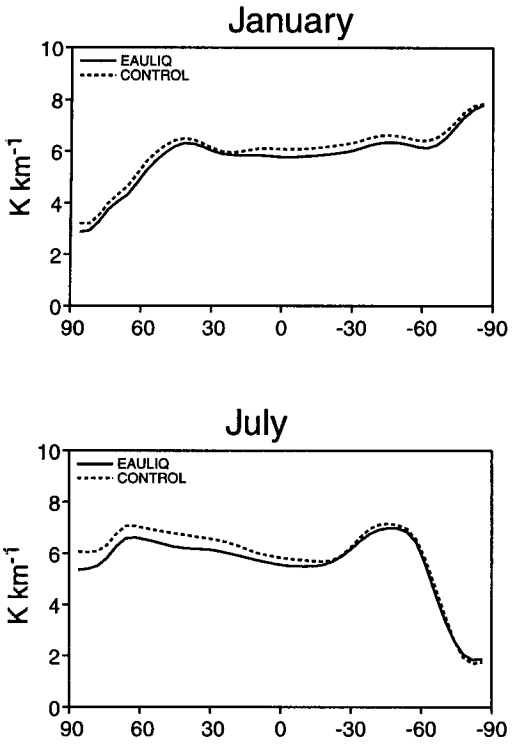

FIG. 17. Zonally averaged distributions of the 300-mb lapse rate simulated by EAULIQ and CONTROL for January and July. Units are in kelvins per kilometer.

reaches values in excess of 20 m s^{-1} in both hemispheres. Also Fig. 22 indicates that the intensity of the subtropical jet is about 10 m s^{-1} weaker in EAULIQ than in CONTROL. Here it is important to note that neither EAULIQ nor CONTROL includes gravity wave drag, which would tend to weaken the westerlies (Palmer et al. 1986). Zonal winds are too weak poleward of 60°S in both simulations. Finally, both EAULIQ and CONTROL underestimate the intensity of the upper-tropospheric easterlies in the Tropics.

The individual contributions of the cumulus convection, moist convective adjustment, and large-scale condensation parameterizations to the total latent heating are discussed in detail in Randall et al. (1989) for a simulation similar to CONTROL. As shown in Fig. 23, the total latent heating rate displays two primary maxima in the Tropics, located at 3 km and 8 km, and two secondary maxima in middle latitudes. In CONTROL, maxima that are observed at the 3-km level in the tropics and middle latitudes result from latent heat release due to cumulus convection and moist convective adjustment. The maximum in the Tropics at the 10-km level results from latent heat release by large-scale condensation. As discussed in Part I, the water detrained at the tops of cumulus towers is assumed to immediately evaporate, hence moistening and cooling the upper-troposphere. The separately parameterized removal of supersaturation by the large-scale condensation parameterization of CONTROL yields a warming and drying of the upper-troposphere so that, in the end, the total latent heating is positive. This unrealistic scenario does not occur in EAULIQ because the condensed water detrained at the tops of cumulus towers is directly used as a source of cloud water and cloud ice for the cloud microphysics scheme. Figure 23 shows that the total latent heating is reduced in the low and upper tropical troposphere and increased in the middle troposphere between EAULIQ and CONTROL because cumulus incidence is significantly reduced in EAULIQ (refer to Fig. 3), and convection does not penetrate as high in EAULIQ as in CONTROL because of the weaker lapse rate (refer to Fig. 17). In middle latitudes, the latent heating of the lower troposphere is increased, especially in the winter hemisphere, due to increased large-scale condensation in EAULIQ.

As shown in Fig. 19, the sum of the net radiative and latent heatings indicates that EAULIQ leads to an overall tropospheric warming except at equatorial latitudes. Outside of the Tropics, the increased warming of the troposphere above 8 km results because of the enhanced net radiative heating between EAULIQ and CONTROL. Below 8 km, the increase in latent heat release explains most of the enhanced tropospheric warming, as can be seen by comparing the relative change in the net radiative and latent heatings between EAULIQ and CONTROL. In the Tropics, the decrease in the diabatic heating results because of the reduced latent heating between EAULIQ and CONTROL. Between the 6-km and 8-km levels, the increase in the diabatic heating results because the increase in latent heating dominates the net radiative cooling due to stratiform anvils. The increased diabatic heating seen above the 16-km level is mostly a radiation effect.

Finally, in Fig. 24, the latitude–height cross sections of the mean meridional circulations obtained with EAULIQ and CONTROL are compared with those obtained from ECMWF observations for July. In both climate simulations, the strong direct Hadley cell in the Tropics and the two weaker indirect Ferrel cells in middle latitudes are clearly seen.[1] Figure 24 reveals that EAULIQ produces a much weaker mean meridional circulation than CONTROL. The intensity of the Hadley cell is decreased by about 100×10^9 kg s^{-1} between the two runs. The weakening of the Hadley cell is consistent with the weakening of penetrative cumulus convection in the Tropics in conjunction with the decreased latent heating and cumulus precipitation there. Comparing our results against the mean meridional circulation computed from ECMWF data, we see that the strength of the Hadley cell is overestimated in

[1] In Fig. 24, clockwise and counterclockwise circulations are indicated by positive and negative values for the streamlines, respectively.

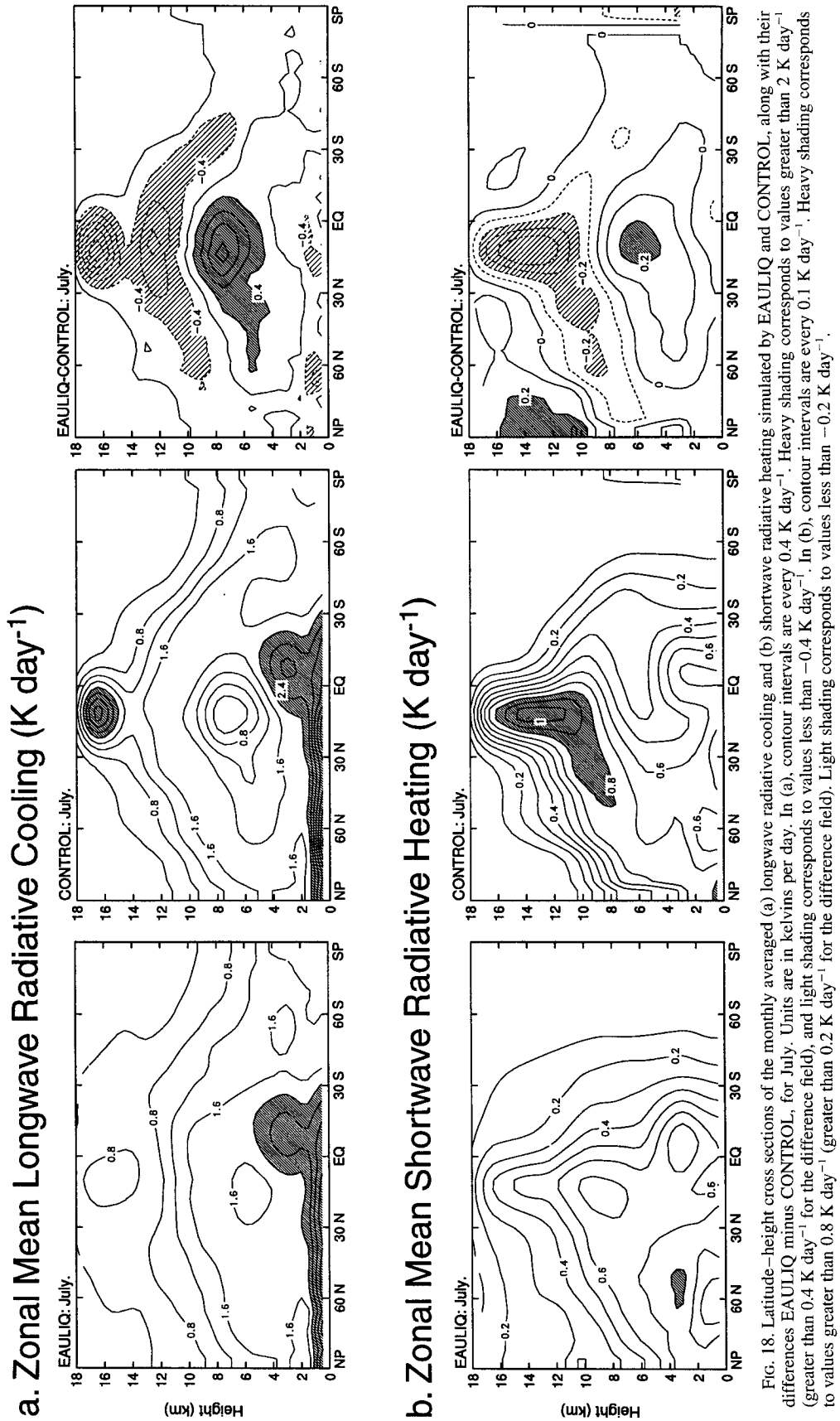

FIG. 18. Latitude–height cross sections of the monthly averaged (a) longwave radiative cooling and (b) shortwave radiative heating simulated by EAULIQ and CONTROL, along with their differences EAULIQ minus CONTROL, for July. Units are in kelvins per day. In (a), contour intervals are every 0.4 K day^{-1}. Heavy shading corresponds to values greater than 2 K day^{-1} (greater than 0.4 K day^{-1} for the difference field), and light shading corresponds to values less than -0.4 K day^{-1}. In (b), contour intervals are every 0.1 K day^{-1}. Heavy shading corresponds to values greater than 0.8 K day^{-1} (greater than 0.2 K day^{-1} for the difference field). Light shading corresponds to values less than -0.2 K day^{-1}.

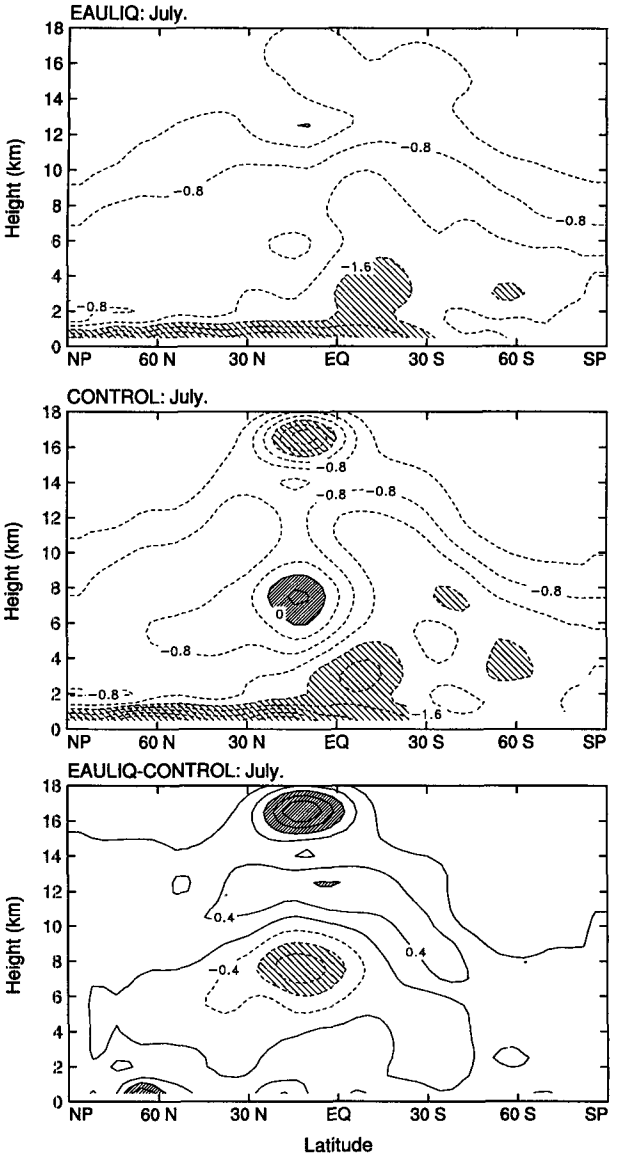

FIG. 19. Latitude–height cross sections of the monthly averaged total radiative heating simulated with EAULIQ, CONTROL, and their difference EAULIQ minus CONTROL, for July. Units are in kelvins per day and contour intervals are every 0.4 K day^{-1}. Heavy shading corresponds to values greater than 0 K day^{-1} (greater than 0.8 K day^{-1} for the difference field). Light shading corresponds to values less than -1.6 K day^{-1} (less than -0.8 K day^{-1} for the difference field).

CONTROL, whereas it is slightly underestimated in EAULIQ.

7. Summary and conclusions

We have compared the climate simulated by the CSU GCM, with and without liquid and ice cloud microphysics, and interactive cloud optical properties. There are large differences between EAULIQ and CONTROL in terms of the distributions of the cloudiness and its optical properties, the planetary radiation budget, and the longwave and shortwave cloud radiative forcings. Also differences between the two runs in the distributions of the radiative and latent heating have a large impact upon the distribution of the temperature, zonal wind, and mean meridional circulation. In terms of the geographical distributions of cloudiness, the longwave and shortwave radiative forcings of clouds, the outgoing infrared radiation, and the planetary albedo, EAULIQ is, in general, in much better agreement with observations than CONTROL, especially in the Tropics. Outside the Tropics, the planetary radiation budget simulated by EAULIQ is not as satisfactory as that simulated by CONTROL. Origins of the discrepancies between EAULIQ and ERBE data are being analyzed in terms of the cloud microphysics parameterization.

EAULIQ produces less high-level cloudiness over the deep tropical convective regions, which in turn leads to a significant improvement in the simulated regional radiation budget and cloud radiative forcings. The changes in the planetary radiation budget and cloud radiative forcing are most dramatic over the western Pacific and Indian Oceans where they lead to a more realistic simulation of the summer and winter monsoons. The changes between CONTROL and EAULIQ are not always an improvement for the simulated atmospheric general circulation.

One key result is that interactions among the cloud microphysics, cumulus, and radiation parameterizations lead to an increased stability of the atmosphere in EAULIQ, especially in the Tropics. The decrease in upper-level clouds and, hence, increase in the outgoing infrared radiation are consistent with the decreased cumulus precipitation discussed in Part I, especially over the monsoon region. Multiple deficiencies remain in the simulation of cloudiness and the longwave and shortwave cloud radiative forcings. For convectively active regions, these problems partially result from an overestimation of upper-level clouds.

Comparisons against circulation statistics indicate that EAULIQ had led to some improvement of the climate simulated by the CSU GCM. We are currently performing a much more detailed comparison of the simulated general circulation of the atmosphere against global observations.

The present version of EAULIQ, including liquid and ice cloud microphysics and interactive cloud optical properties, has two major weaknesses. First, the parameterization does not include fractional cloudiness. Second, the CSU GCM does not include an adequate parameterization of planetary boundary-layer clouds, which hinders, in particular, a satisfactory simulation of the shortwave cloud radiative forcing over the Southern Ocean and along the western coasts of the continents. Parameterization of fractional cloudiness as a function of the grid-averaged

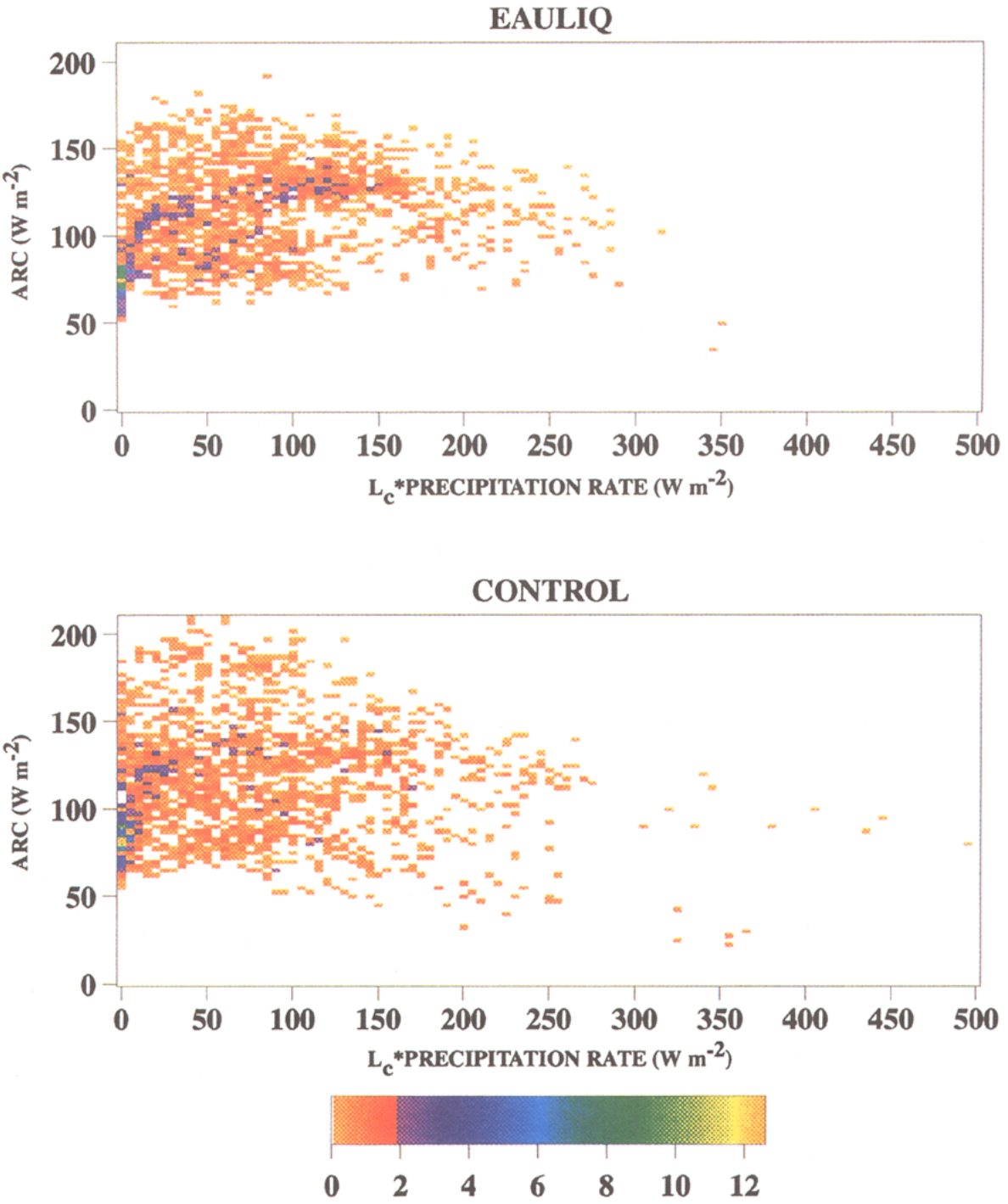

FIG. 20. Probability density function of the precipitation rate times the latent heat of condensation (L_c) versus the atmospheric radiative cooling simulated by EAULIQ and CONTROL for July. Units are in watts per square meter.

cloud water and cloud ice paths and the large-scale relative humidity is under development, following the work of Xu and Randall (1994). An improved parameterization of PBL clouds is also a high priority, following Randall et al. (1992).

Acknowledgments. This research was sponsored by the National Science Foundation under Grant ATM-8907414, NASA under Grant NAG-1-1266, and by the ARM program of the U.S. Department of Energy under Grant DE-FG02-92ER61363, all to Colorado

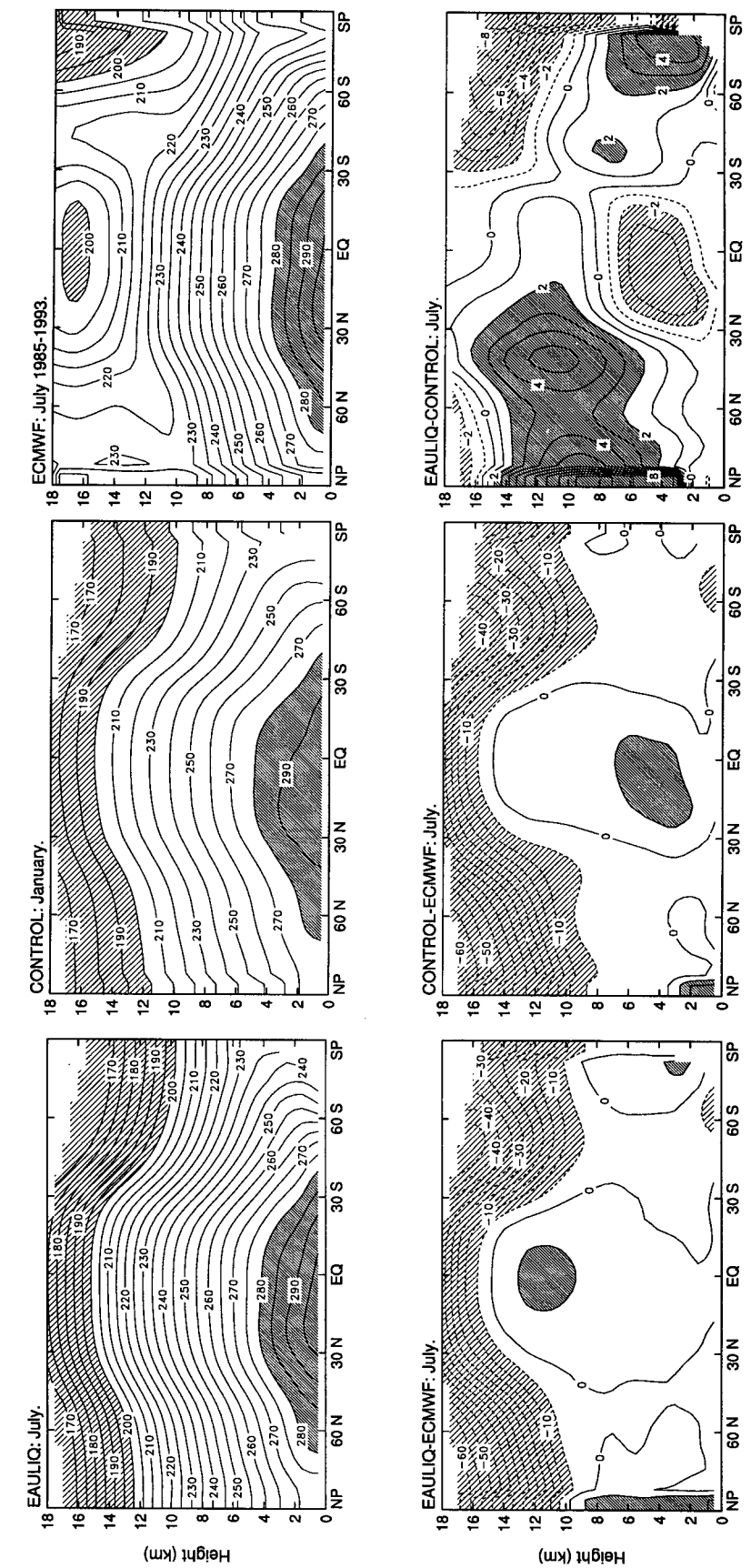

FIG. 21. Latitude–height cross sections of the monthly averaged temperature simulated with EAULIQ and CONTROL, obtained from ECMWF data, along with the differences EAULIQ minus ECMWF, CONTROL minus ECMWF, and EAULIQ minus CONTROL, for July. Units are in Kelvins and contour intervals are every 10 K (every 5 K for the differences EAULIQ minus ECMWF and CONTROL minus ECMWF and every 1 K for the difference EAULIQ minus CONTROL). Heavy shading corresponds to values greater than 280 K (greater than 5 K for the differences EAULIQ minus ECMWF and CONTROL minus ECMWF and greater than 2 K for the difference EAULIQ minus CONTROL). Light shading corresponds to values less than 200 K (less than 5 K for the differences EAULIQ minus ECMWF and CONTROL minus ECMWF and less than −2 K for the difference EAULIQ minus CONTROL).

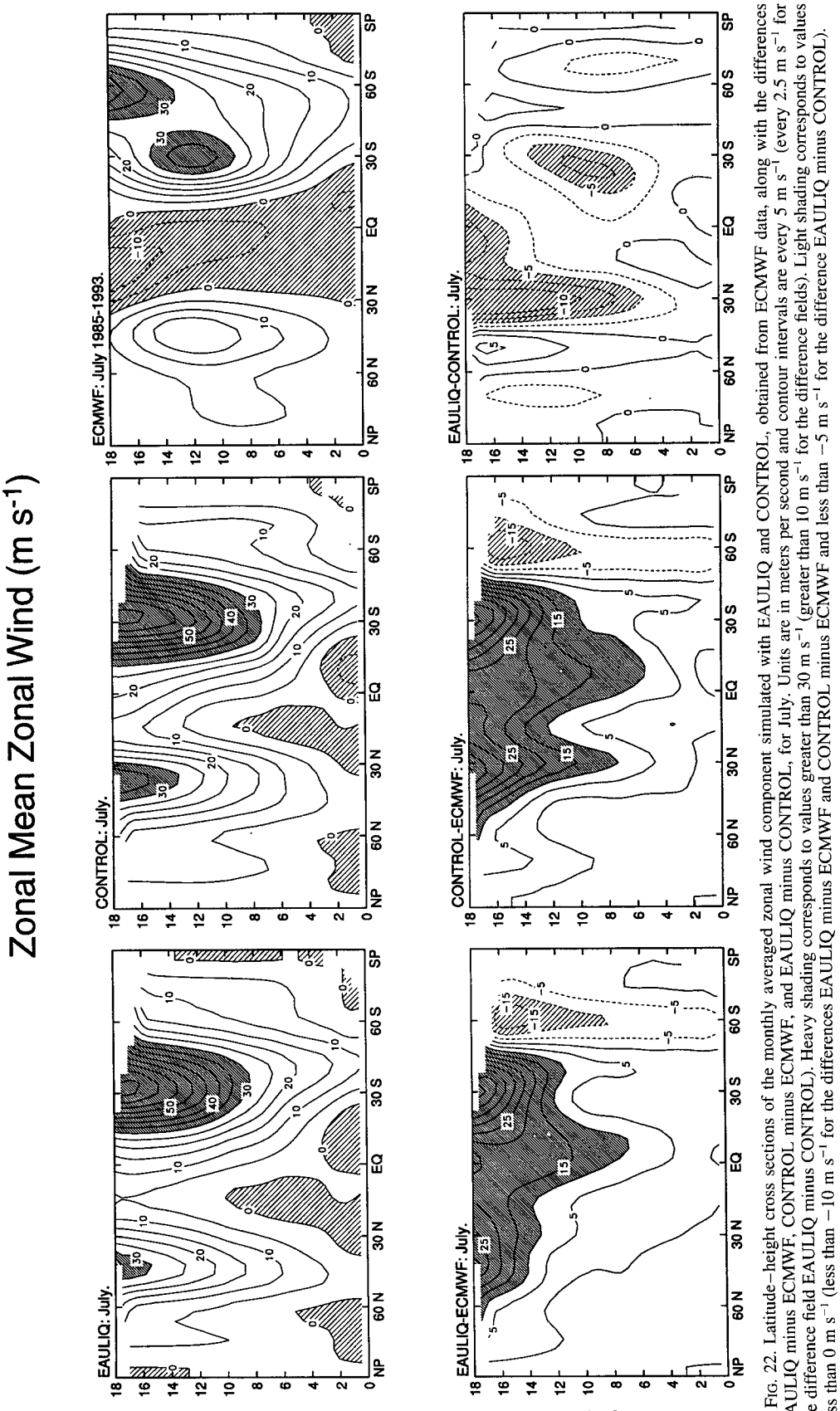

FIG. 22. Latitude–height cross sections of the monthly averaged zonal wind component simulated with EAULIQ and CONTROL, obtained from ECMWF data, along with the differences EAULIQ minus ECMWF, CONTROL minus ECMWF, and EAULIQ minus CONTROL, for July. Units are in meters per second and contour intervals are every 5 m s^{-1} (every 2.5 m s^{-1} for the difference field EAULIQ minus CONTROL). Heavy shading corresponds to values greater than 30 m s^{-1} (greater than 10 m s^{-1} for the difference fields). Light shading corresponds to values less than 0 m s^{-1} (less than -10 m s^{-1} for the differences EAULIQ minus ECMWF and CONTROL minus ECMWF and less than -5 m s^{-1} for the difference EAULIQ minus CONTROL).

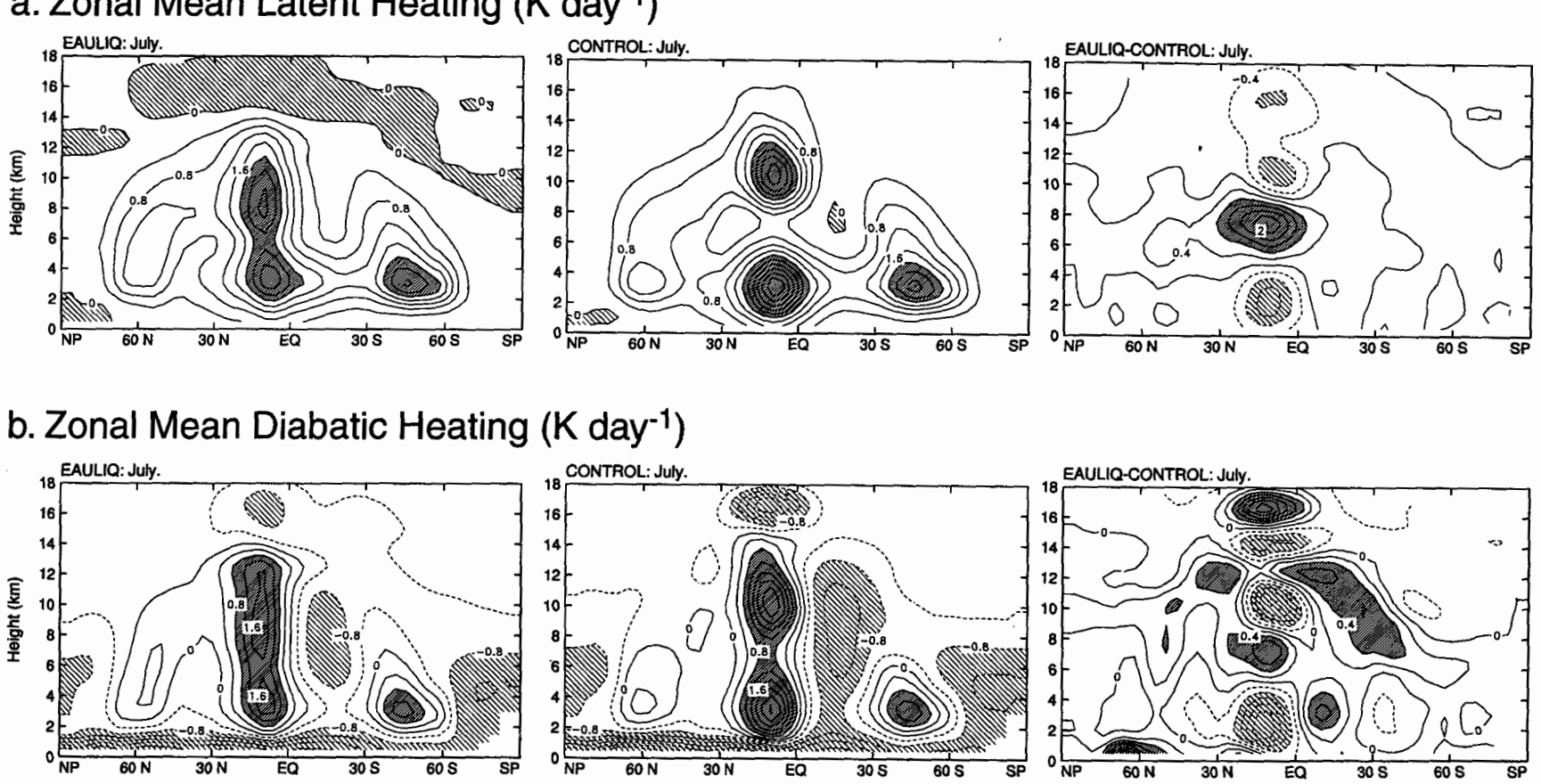

FIG. 23. Latitude–height cross sections of the monthly averaged (a) latent heating and (b) diabatic heating simulated by EAULIQ and CONTROL, along with their differences EAULIQ minus CONTROL, for July. Units are in kelvins per day. In (a), contour intervals are every 0.4 K day^{-1}. Heavy shading corresponds to values greater than 2 K day^{-1} (greater than 0.8 K day^{-1} for the difference field). Light shading corresponds to values less than 0 (less than -0.8 K day^{-1} for the difference field). In (b), contour intervals are every 0.4 K day^{-1} (0.2 K day^{-1} for the difference field). Heavy shading corresponds to values greater than 0.8 K day^{-1} (greater than 0.4 K day^{-1} for the difference field). Light shading corresponds to values less than -0.8 K day^{-1}.

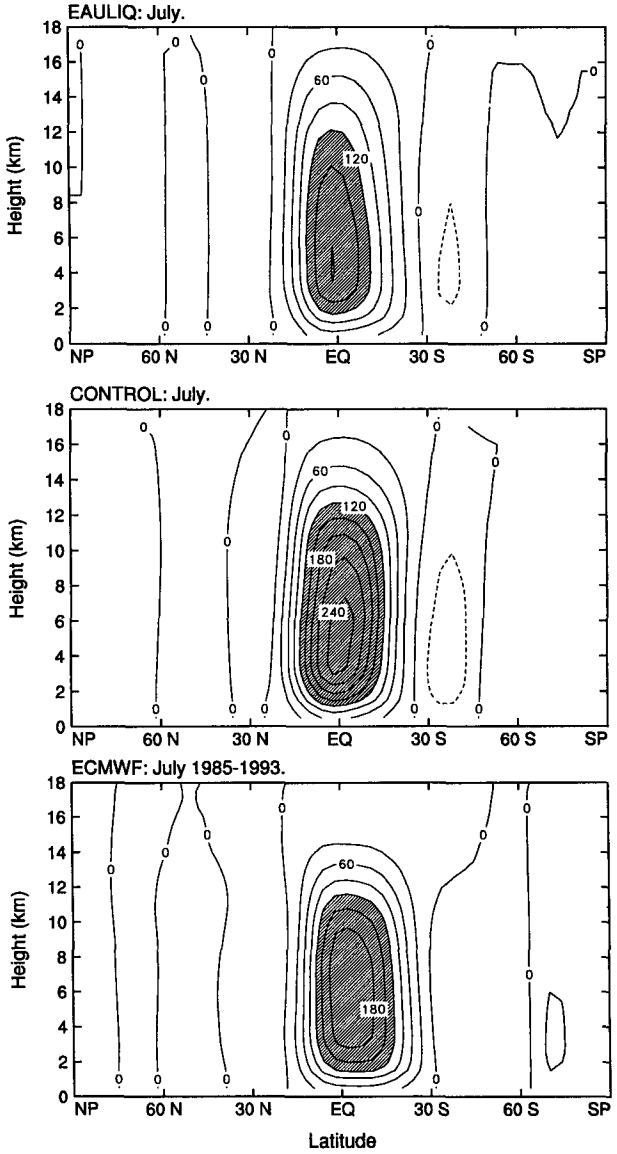

FIG. 24. Latitude–height cross sections of the monthly averaged mean meridional circulation simulated with EAULIQ and CONTROL, derived from ECMWF data, for July. Units are in 10^9 kg s^{-1} and contour intervals are every 30×10^9 kg s^{-1}. Light shading corresponds to values less than -30×10^9 kg s^{-1}, and heavy shading corresponds to values greater than 120×10^9 kg s^{-1}.

State University, and by subcontract 0965G4A007 from the University of California at Los Angeles, California, under NASA Grant NAG 5-2224 to UCLA. Computing resources were provided by the Scientific Computing Division at the National Center for Atmospheric Research, by the National Center for Computational Sciences at NASA/Goddard and by the National Energy Research Supercomputer Center at Lawrence Livermore National Laboratory. We would like to thank D. Dazlich, also of the Department of Atmospheric Science at Colorado State University, for his invaluable assistance in working with the CSU GCM in the early stages of this research.

REFERENCES

Arakawa, A., and W. H. Schubert, 1974: The interactions of a cumulus cloud ensemble with the large-scale environment. Part I. *J. Atmos. Sci.*, **31,** 674–701.

Barkstrom, B. R., and G. L. Smith, 1986: The Earth Radiation Budget Experiment: Science and implementation. *J. Geophys. Res.*, **24,** 379–390.

Cess, R. D., and G. L. Potter, 1987: Exploratory studies of cloud radiative forcing with a general circulation model. *Tellus,* **39A,** 460–473.

Charlock, T. P., and V. Ramanathan, 1985: The albedo field and cloud radiative forcing produced by a general circulation model with internally generated cloud optics. *J. Atmos. Sci.*, **42,** 1408–1429.

Chou, M. D., 1984: Broadband water vapor transmission functions for atmospheric IR flux computations. *J. Atmos. Sci.*, **41,** 1775–1778.

——, and L. Peng, 1984: A parameterization of the absorption in the 15 μm CO_2 spectral region with application to climate sensitivity studies. *J. Atmos. Sci.*, **32,** 409–418.

Del Genio, A. D., and M.-S Yao, 1988: Sensitivity of a global climate model to the specification of convective updraft and downward mass fluxes. *J. Atmos. Sci.*, **45,** 2641–2668.

Ebert, E. E., and J. A. Curry, 1992: A parameterization of ice cloud optical properties for climate models. *J. Geophys. Res.*, **97,** 3831–3836.

Fowler, L. D., D. A. Randall, and S. A. Rutledge, 1996: Liquid and ice cloud microphysics in the CSU general circulation model. Part I: Model description and results of a baseline simulation. *J. Climate,* **9,** 489–529.

Garratt, J. R., 1994: Incoming shortwave fluxes at the surface—a comparison of GCM results with observations. *J. Climate,* **7,** 72–80.

——, P. B. Krummel, and E. A. Kowalczyk, 1993: The surface energy balance at local and regional scales—a comparison of general circulation model results with observations. *J. Climate,* **6,** 1090–1109.

Gupta, S. K., W. F. Staylor, W. L. Darnell, A. C. Wilber, and N. A. Ritchey, 1993: Seasonal variations of surface and cloud radiative forcing over the globe derived from satellite data. *J. Geophys. Res.*, **98,** 20 761–20 778.

Harshvardhan, R. Davies, D. A. Randall, and T. G. Corsetti, 1987: A fast radiation parameterization for atmospheric general circulation models. *J. Geophys. Res.*, **92,** 1009–1016.

——, D. A. Randall, T. G. Corsetti, and D. A. Dazlich, 1989: Earth radiation budget and cloudiness simulations with a general circulation models. *J. Atmos. Sci.*, **46,** 1922–1942.

Hollingsworth, A., D. B. Shaw, P. Lönnberg, L. Illam, K. Arpe, and A. J. Simmons, 1986: Monitoring of observations and analysis quality by a data assimilation system. *Mon. Wea. Rev.*, **114,** 861–879.

Hu, Y. X., and K. Stamnes, 1993: An accurate parameterization of the radiative properties of water clouds suitable for use in climate models. *J. Climate,* **6,** 728–742.

Joseph, J. H., W. J. Wiscombe, and J. A. Weinman, 1976: The Delta–Eddington approximation for radiative flux transfer. *J. Atmos. Sci.*, **33,** 2452–2459.

Lacis, A. A., and J. E. Hansen, 1974: A parameterization for the absorption of solar radiation in the earth's atmosphere. *J. Atmos. Sci.*, **31,** 118–133.

Le Treut, H., and Z.-X. Li, 1988: Using Meteosat data to validate a prognostic cloud generation scheme. *Atmos. Res.*, **21,** 273–292.

Li, Z., and H. G. Leighton, 1993: Global climatologies of solar radiation budgets at the surface and in the atmosphere from 5 years of ERBE data. *J. Geophys. Res.*, **98,** 4919–4930.

Lin, Y.-L., R. D. Farley, and H. D. Orville, 1983: Bulk parameterization of the snow field in a cloud model. *J. Climate Appl. Meteor.*, **22,** 1065–1092.

Manabe, S., J. Smagorinsky, and R. F. Strickler, 1965: Simulated climatology of a general circulation model with a hydrological cycle. *Mon. Wea. Rev.*, **93,** 769–798.

Ose, T., 1993: An examination of the effects of explicit cloud water in the UCLA GCM. *J. Meteor. Soc. Japan,* **71,** 93–109.

Palmer, T. N., G. J. Shutts, and R. Swinbank, 1986: Alleviation of a systematic westerly bias in general circulation and numerical weather prediction models through an orographic gravity wave parameterization. *Quart. J. Roy. Meteor. Soc.,* **112,** 1001–1039.

Platt, C. M. R., and Harshvardhan, 1988: Temperature dependence of cirrus extinction—implications for climate feedback. *J. Geophys. Res.*, **93,** 11 051–11 058.

Ramanathan, V., 1987: The role of Earth Radiation Budget studies in climate and general circulation research. *J. Geophys. Res.,* **92,** 4075–4094.

——, E. J. Pitcher, R. C. Malone, and M. L. Blackmon, 1983: The response of a spectral general circulation model to refinements in radiative processes. *J. Atmos. Sci.,* **40,** 605–630.

Randall, D. A., and D.-M. Pan, 1993: Implementation of the Arakawa–Schubert cumulus parameterization with a prognostic closure. *The Representation of Cumulus Convection in Numerical Models Meteor. Monogr.,* No. 46 Amer. Meteor. Soc., 137–144.

——, Harshvardhan, D. A. Dazlich, and T. G. Corsetti, 1989: Interactions among radiation, convection, and large-scale dynamics in a general circulation model. *J. Atmos. Sci.,* **46,** 1943–1970.

——, ——, and ——, 1991: Diurnal variability of the hydrological cycle in a general circulation model. *J. Atmos. Sci.,* **48,** 40–62.

——, Q. Shao, and C.-H. Moeng, 1992: A second-order boundary layer model. *J. Atmos. Sci.,* **49,** 1903–1923.

Roberts, R. E., J. E. A. Selby, and L. Biberman, 1976: Infrared continuum absorption by atmospheric water vapor in the 8–12 μm window. *Appl. Opt.,* **5,** 2085–2090.

Rockel, B., E. Raschke, and B. Weyres, 1991: A parameterization of broadband radiative transfer properties of water, ice, and mixed clouds. *Contrib. Atmos. Phys.,* **64,** 1–12.

Rodgers, C. D., 1968: Some extensions and applications of the new random model for molecular band transmission. *Quart. J. Roy. Meteor. Soc.,* **94,** 99–102.

Roeckner, E., M. Rieland, and E. Keup, 1990: Modelling of clouds and radiation in the ECHAM model. *Proc. of ECMWF/WCRP Workshop on Clouds, Radiation, and the Hydrologic Cycle,* Reading, UK, ECMWF, 199–222.

Rossow, W. B., and R. A. Schiffer, 1983: The International Satellite Cloud Climatology Project (ISCCP): The first project of the World Climate Research Program. *Bull. Amer. Meteor. Soc.,* **64,** 779–784.

——, and ——, 1991: ISCCP cloud data products. *Bull. Amer. Meteor. Soc.,* **72,** 2–20.

Rutledge, S. A., and P. V. Hobbs, 1983: The mesoscale and microscale structure and organization of clouds and precipitation in midlatitude cyclones. VIII: A model for the "seeder–feeder" process in warm-frontal rainbands. *J. Atmos. Sci.,* **40,** 1185–1206.

——, and ——, 1984: The mesoscale and microscale structure and organization of clouds and precipitation in midlatitude cyclones. XII: A diagnostic modeling study of precitation development in narrow cold-frontal rainbands. *J. Atmos. Sci.,* **41,** 2949–2972.

Senior, C. A., and J. F. B. Mitchell, 1993: Carbon dioxide and climate: The impact of cloud parameterization. *J. Climate,* **6,** 393–417.

Slingo, A., 1989: A GCM parameterization for the shortwave radiative properties of water clouds. *J. Atmos. Sci.,* **46,** 1419–1427.

Smith, R. N. B., 1990: A scheme for predicting layer clouds and their water content in a general circulation model. *Quart. J. Roy. Meteor. Soc.,* **116,** 435–460.

Stephens, G. L., 1978: Radiation profiles in extended water clouds. Part II: Parameterization schemes. *J. Atmos. Sci.,* **35,** 2123–2132.

Suarez, M. J., A. Arakawa, and D. A. Randall, 1983: Parameterization of the planetary boundary layer in the UCLA general circulation model: Formulation and results. *Mon. Wea. Rev.,* **111,** 2224–2243.

Sun, Z., and K. P. Shine, 1994: Studies of the radiative properties of ice and mixed-phase clouds. *Quart. J. Roy. Meteor. Soc.,* **120,** 111–137.

Tiedke, M., 1993: Representation of clouds in large-scale models. *Mon. Wea. Rev.,* **121,** 3040–3061.

Trenberth, K. E., and J. G. Olson, 1988: An evaluation and intercomparison of global analyses from the National Meteorological Center and the European Centre for Medium-Range Weather Forecasts. *Bull. Amer. Meteor. Soc.,* **69,** 1047–1057.

Xu, K-M., and D. A. Randall, 1994: Further development of a cloud parameterization for use in climate models with ARM data. *Fifth Symp. on Global Change Studies.* Nashville, TN, Amer. Meteor. Soc., 6–10.